NITROGEN OXIDES ABATEMENT FROM FLUE GAS VIA NON-THERMAL PLASMA

MR. PHURIN CHONPAN

A THESIS SUBMITTED IN PARTIAL FULFILLMENT OF THE REQUIREMENTS
FOR THE DEGREE OF MASTER OF ENGINEERING IN
AUTOMOTIVE AND ENERGY ENGINEERING TECHNOLOGY
DEPARTMENT OF POWER ENGINEERING TECHNOLOGY
GRADUATE COLLEGE
KING MONGKUT'S UNIVERSITY OF TECHNOLOGY NORTH BANGKOK
ACADEMIC YEAR 2025

NITROGEN OXIDES ABATEMENT FROM FLUE GAS VIA NON-THERMAL PLASMA

MR. PHURIN CHONPAN

A THESIS SUBMITTED IN PARTIAL FULFILLMENT OF THE REQUIREMENTS
FOR THE DEGREE OF MASTER OF ENGINEERING IN
AUTOMOTIVE AND ENERGY ENGINEERING TECHNOLOGY
DEPARTMENT OF POWER ENGINEERING TECHNOLOGY
GRADUATE COLLEGE
KING MONGKUT'S UNIVERSITY OF TECHNOLOGY NORTH BANGKOK
ACADEMIC YEAR 2025

Thesis Proposal Certificate

The Graduate College, King Mongkut's University of Technology North Bangkok

Title NITROGEN OXIDES ABATEMENT FROM FLUE GAS VIA NON-THERMAL PLASMA

By Mr. Phurin Chonpan

Accepted by the COLLEGE OF INDUSTRIAL TECHNOLOGY, King Mongkut's University of Technology North Bangkok in Partial Fulfillment of the Requirements for the Master of Engineering in Power Engineering Technology

..... Dean / Head of Department

(Assistant Professor Dr. Suphot Chunwiphat)

Thesis Examination Committee

..... Chairperson

(Assistant Professor Dr. Attaphon Chaimanatsakun)

..... Advisor

(Assistant Professor Dr. Sak Sittichompoo)

..... Co-Advisor

(Associate Professor Dr. Kampanart Theinnoi)

..... Committee

(Associate Professor Dr. Boonlue Sawatmongkol)

Name : Mr. Phurin Chonpan
Thesis Title : NITROGEN OXIDES ABATEMENT FROM FLUE GAS VIA NON-THERMAL PLASMA
Major Field : Automotive and Energy Engineering Technology
King Mongkut's University of Technology North Bangkok
Thesis Advisor : Assistant Professor Dr. Sak Sittichompoo
Co-Advisor : Associate Professor Dr. Kampanart Theinnoi
Academic Year : 2025

ABSTRACT

This research investigated the use of dielectric-barrier-discharge non-thermal plasma (DBD-NTP) for nitrogen oxide (NO_x) abatement in flue-gas applications, combining ozone generation and its subsequent utilisation for NO oxidation. A systematic experimental was conducted, comprising verification of the inverted tracer-gas method, evaluation of ozone-generation characteristics under various discharge parameters, up-scaling of multi-cell reactors, and ozone-assisted oxidation of NO in real diesel-flue-gas streams. The inverted tracer-gas technique was validated as a reliable and economical approach for determining volumetric flow rates, maintaining strong linearity ($R^2 \approx 0.99$) across 25–210 °C. Ozone generation was strongly influenced by discharge voltage, frequency, oxygen concentration, and gas-flow rate. The three-cell reactor achieved 11946 ppm ozone and 0.29 g/min production rate, while the two-cell configuration revealed the highest overall energy efficiency (6.21 μg/J). In real flue-gas experiments, ozone injection effectively converted NO to NO_2, achieving up to 50 % conversion with 0.815 μg/J efficiency at optimal conditions ($O_3/NO \approx 2.35$).

These findings demonstrate that DBD-NTP technology provides a low-temperature, modular, and scalable approach for plasma-assisted NO_x control. Integration of ozone pre-oxidation with catalytic after-treatment offers a practical pathway toward enhanced $DeNO_x$ efficiency and reduced energy consumption in industrial exhaust systems.

(Total 59 Pages)

Keywords : NTP, DBD, ozone generation, NO oxidation and inverted tracer gas

_____ Advisor

ACKNOWLEDGEMENTS

For their invaluable supervision, ongoing guidance, and constructive feedback throughout this research, the author would like to thank sincerely. Asst. Prof. Dr. Sak Sittichompoo, Assoc. Prof. Dr. Kampanart Theinnoi, Assoc. Prof. Dr. Boonlue Sawatmongkhon, and Assoc. Prof. Dr. Thawatchai Wongchang. Their knowledge and support were crucial to this work's successful completion.

Special thanks are extended to the Research Centre for Combustion Technology and Alternative Energy (CTAE), King Mongkut's University of Technology North Bangkok (KMUTNB), for providing essential research facilities, laboratory instrumentation, and technical support. The author also gratefully acknowledges the College of Industrial Technology (CIT), KMUTNB, for funding this study under the graduate scholarship Contract No. CIT-2023-GRAD-29.

The author expresses heartfelt appreciation to fellow researchers and laboratory colleagues for their assistance, collaboration, and encouragement throughout the experimental and analytical stages of this work, especially Dr. Punya Promhuad, whose generous guidance and insightful suggestions were greatly valued. Finally, the author wishes to dedicate deep gratitude to his family and loved ones for their unwavering support, understanding, and motivation throughout the course of his graduate study and research journey.

Phurin Chonpan

TABLE OF CONTENTS

Page

TABLE OF CONTENTS(CONTINUED)

LIST OF TABLES

Page

LIST OF FIGURES

Page

LIST OF FIGURES(CONTINUED)

Page

LIST OF ABBREVIATIONS

Abbreviation / Symbol	Description
$\%C_{CO_{2,0}}$	CO_2 before dilution (%-Vol.)
$\%C_{CO_{2,1}}$	CO_2 after dilution (%-Vol.)
DBD	Dielectric barrier discharge
DBD-NTP	Dielectric barrier discharge non-thermal plasma
$DeNO_x$	Nitrogen oxides removal
DSO	Digital storage oscilloscope
f	Frequency (Hz)
FTIR	Fourier transform infrared spectroscopy
GHSV	Gas hourly space velocity
HVPS	High-voltage power supply
I	Current (A)
N_2O	Nitrous oxide
N_2O_5	Dinitrogen pentoxide
NO	Nitric oxide
NO_2	Nitrogen dioxide
NO_3	Nitrogen trioxide
NO_x	Nitrogen Oxides
NTP	Non-thermal plasma
O_3	Ozone
OPE	Ozone production efficiency (µg/J)
OPR	Ozone production rate (g/min)
P_D	Discharge power (W)
P_m	Measured or total input power (W)
q	Gas flow rate (LPM)
Q	Electric charge (C)
R^2	Coefficient of determination
SED	Specific energy density (J/L, referenced to discharge power)
SEI	Specific energy input (J/L, referenced to discharge power)
SOEI	Specific overall energy input (J/L, referenced to total input power)
SOPE	System ozone production efficiency (µg/J)
t	Time (s)
V_{pp}	Peak-to-peak voltage (V)

CHAPTER 1
INTRODUCTION

1.1 Theoretical background

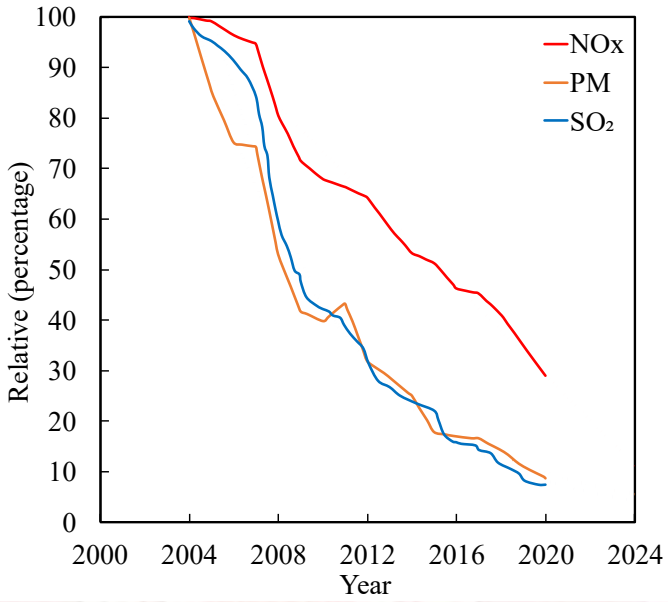

FIGURE 1-1 Emission of PM, NO_x and SO_2 from large combustion plants in the EU-27 [1].

Nowadays, the growth of industry and the economy contribute to a significant increase in energy consumption. The International Energy Agency (IEA) estimates that worldwide energy consumption, specifically in the form of electricity, will increase by 53% in 2023 [2]. Fossil fuels including coal, natural gas, diesel, and fuel oil remain the primary fuel sources for electricity generation. However, the combustion of these resources leads to the release of harmful pollutants such a, particulate matter (PM), nitrogen oxides (NO_x), etc. Carbon dioxide (CO_2) is the main greenhouse gas (GHG) that contributes to global warming [3], as it absorbs infrared radiation in the atmosphere and traps heat within the Earth's climate system. At the same time, PM poses significant adverse effects on human health by affecting the respiratory system, a probable cause of lung cancer [4,5], and shorter life expectancy [6]. NO_x emission consists of nitric oxide (NO) and nitrogen dioxide (NO_2). Emissions of NO_x can lead to a range of health problems, such as irritation of the eyes and throat and headaches. Moreover, NO_x emissions can contribute to environmental issues, causing photochemical smog and acid rain formation [7,8]. Photochemical smog primarily consists of secondary pollutants such as ozone (O_3) and peroxyacetyl nitrates (PANs), which are formed through sunlight-driven reactions between NO_x and volatile organic compounds (VOCs). These oxidants degrade air quality, reduce visibility, and pose serious health risks to humans and the environment. Exposure to these air pollutants, particularly O_3 and PANs, is associated with increased incidences of respiratory and cardiovascular diseases, posing significant threats to public health and urban air quality [9]. Sulphur dioxide (SO_2) and NO_x act as key precursors of acid rain through their reactions with water vapour and other atmospheric constituents, where NO_x is converted into nitric

acid (HNO_3). The acidic precipitation that results from this process makes soils and surface waters more acidic, which harms ecosystems, plants, and buildings and infrastructure [10].

According to those mentioned above, stricter limits on pollutant emissions are required to maintain natural equilibrium, as shown in FIGURE 1-1, EU-27 policies are expected to drive further reductions in combustion plant emissions in the coming years [1]. Reducing NO_x is critical because it has a significant impact on the environment and public health.

There are three methods of controlling NO_x emissions in external combustion, namely pre-combustion, in-combustion, and post-combustion [11]. The pre-combustion method focuses on minimising nitrogen in the fuel, specifically by selecting a fuel with a low nitrogen content or lowering the nitrogen content of the fuel. The in-combustion control method, also known as low-NO_x combustion technology, is primarily used to reduce NO_x emissions by adjusting the parameters of operation and modifying the combustion process. Flue gas recirculation (FGR) is a method for lowering NO_x ($DeNO_x$) by reintroducing flue gases from the exhaust of the combustor into the intake air. FGR is an effective approach for NO reduction, however, the heat transfer efficiency is reduced due to a lower temperature [12]. Water injection is a method which injects water into the combustion zone. The presence of water in the combustion zone reduces NO_x generation by lowering the flame temperature [13]. However, water causes corrosion, resulting in the premature breakdown of metal parts of the combustion chamber. Several research have been carried out to develop realisable post-combustion technologies and more effective approaches to meet the stringent environmental regulations for NO_x.

Selective non-catalytic reduction (SNCR) and selective catalytic reduction (SCR) are the principal post-combustion technologies employed for NO_x reduction [11]. In the SNCR process, ammonia (NH_3) or urea (NH_2CONH_2) solution (e.g. AUS32) is injected directly into the flue gas without a catalyst [14]. Within a narrow high-temperature range of approximately 800 °C, NH_3 reacts with NO_x to form nitrogen (N_2) and water vapour (H_2O) [15]. However, because of its strong temperature dependence and the absence of a catalyst, SNCR generally exhibits lower NO_x removal efficiency compared with catalytic systems and is often unsuitable for low-temperature flue gas streams. The SCR process overcomes these limitations by introducing a catalyst that enables the same reduction reactions to proceed effectively at lower temperatures, typically around 300 °C [16]. In this system, NH_3, hydrocarbons (C_xH_y), CO, or H_2 are injected into the flue gas, where they react with NO_x on the catalyst surface, converting NO_x into N_2 and H_2O [17]. Although NH_3-SCR demonstrates high removal efficiency, several operational issues remain such as ammonia slip, catalyst deactivation, storage and handling hazards, corrosion, odour formation, and substantial capital and maintenance costs [11,18]. The SCR process typically proceeds through three principal reaction pathways, such as standard SCR, fast-SCR, and NO_2-SCR for converting NO_x into N_2 and water via distinct mechanisms. Among these, the fast-SCR pathway exhibits the highest reaction rate, proceeding up to ten times faster when the molar ratio of NO to NO_2 is approximately 1 (NO/NO_2 = 1:1) [19]. This highlights the importance of promoting NO oxidation to NO_2 in the flue gas before catalytic reduction, as this pre-oxidation can significantly enhance SCR efficiency. One effective method to generate

the necessary oxidising species, such as O_3, is through plasma technology, which offers a high capacity for large-scale O_3 production [20].

Plasma is the fourth state of substance [21], referred to when electrical energy is delivered to electrons, activating a release of free radicals such as NO, O, HO_2, and OH [22]. The process releases light as a result. Plasma can be classified as thermal plasma or non-thermal plasma (NTP) depending on whether the heat balance is achieved. NTP, as the name suggests, refers to plasma in which the average energy of electrons is significantly higher than that of ions and gases. NTP can be generated in five ways: glow discharge, corona discharge, dielectric barrier discharge, radio frequency discharge, and microwave discharge [23,24]. The dielectric barrier discharge non-thermal plasma (DBD-NTP) is constructed by placing dielectric barrier material between two electrodes, which is designed to avoid spark discharge. At least one electrode must be covered with a dielectric material [25].

Accurately quantifying gaseous emissions in mass units is challenging due to the simultaneous presence of high concentrations of particulate matter (PM) and water vapour, which can interfere with both concentration and flow measurements. Determining the total volumetric flow rate typically relies on velocity-based instruments such as Pitot tubes [26], hot-wire anemometers [27], ultrasonic flow meters [28], and orifice plates [29] estimate velocity from pressure based on Bernoulli's principle [32]. However, these velocity-based methods are often limited by non-ideal flow profiles, turbulence, and geometric constraints that compromise measurement accuracy [30-32]. In contrast, the tracer-gas dilution method determines total flow directly from gas-phase mixing. By introducing a known quantity of inert tracer gas—commonly helium (He), sulphur hexafluoride (SF_6), nitrous oxide (N_2O), or hexafluorobenzene (C_6F_6) into the gas stream, the degree of dilution downstream can be used to determine the total volumetric flow rate with high accuracy.[33-35]. This approach is less sensitive to asymmetry and duct geometry and has demonstrated accuracy in large-scale exhaust systems [36]. Nonetheless, its implementation requires suitable tracer selection and high-sensitivity analysers, which increase operational complexity and cost.

This thesis aims to investigate a dielectric barrier discharge non-thermal plasma (DBD-NTP) system for the abatement of nitrogen oxides (NO_x) from flue gas. The research primarily focuses on a comprehensive study of ozone generation under various operating parameters, including the up-scaling of the DBD-NTP reactor system. Furthermore, it evaluates the oxidation of nitric oxide (NO) in both simulated and real diesel flue gas using plasma-generated ozone. A secondary objective involves verifying the accuracy of the inverted tracer-gas method for flow-rate measurement in the simulated flue-gas system. The outcomes of this study provide a scientific foundation for integrating plasma-based ozone generation into hybrid $DeNO_x$ systems and contribute to the advancement of cleaner and more sustainable emission-control technologies.

1.2 Objective

1.2.1 Investigate ozone generation using a DBD-NTP system under various operating conditions.

1.2.2 Investigate the oxidation of NO to NO_2 by plasma-generated ozone and evaluate the reaction characteristics

1.2.3 To develop and evaluate an up-scaled DBD-NTP reactor for enhanced performance in ozone production.

1.3 Scope

1.3.1 GHSV = 30000 h^{-1}or greater was utilised.

1.3.2 High voltage between 10 to 40 kV (Voltage peak to peak) is used with a frequency between 50 - 500 Hz.

1.3.3 Specific energy density (SED) of 10 – 700 J/L, corresponding to the discharge energy range for ozone generation applied to NO_x removal ($DeNO_x$).

1.3.4 The DBD-NTP reactor is designed based on the cylindrical configuration.

1.3.5 Flue gas is generated from a diesel oil burner.

1.4 Expected benefits

1.4.1 This innovative approach has the potential to be widely adopted in various industrial applications, offering a substantial improvement in air quality, thereby positively impacting people's well-being and health.

1.4.2 The application of non-thermal plasma is expected to play an important role in supporting power plants and the industrial sector in fulfilling and complying with stringent pollution emission regulations.

1.4.3 The outcomes of this research are expected to strengthen the industrial sector’s transition towards Industry 4.0 by promoting the adoption of advanced, energy-efficient, and sustainable emission-control technologies that enhance both environmental performance and industrial competitiveness.

CHAPTER 2
LITERATURE REVIEW AND RELATED RESEARCH

This chapter presents a detailed review of literature relevant to nitrogen oxides (NO_x) and plasma-assisted emission control. It begins by outlining the fundamental characteristics of NO_x, followed by an examination of the principal NO_x formation mechanisms in combustion. The chapter then discusses the environmental and health impacts associated with NO_x exposure and summarises key national and international regulatory limits. Conventional mitigation methods—such as Selective Catalytic Reduction (SCR) and Selective Non-Catalytic Reduction (SNCR) are reviewed, after which attention is directed to the oxidation of NO to NO_2 by ozone and its importance for enhancing fast-SCR reactions. Subsequent sections provide an in-depth review of plasma technologies relevant to NO_x control and ozone generation. Finally, the chapter addresses techniques for measuring flue-gas volumetric flow rate, which are essential for accurate evaluation of pollutant concentrations and overall reaction performance.

2.1 Characteristics of nitrogen oxides (NO_x)

TABLE 2-1 Family of Nitrogen oxides [37].

Formula	Name	Valence	Properties
N_2O	Nitrous oxide	1	colorless gas water-soluble
NO N_2O_2	Nitric oxide Dinitrogen dioxide	2	colorless gas slightly water soluble
N_2O_3	Dinitrogen trioxide	3	black solid water-soluble decomposes in water
NO_2 N_2O_4	Nitrogen dioxide Dinitrogen tetroxide	4	red-brown gas, very water soluble, decomposes in water
N_2O_5	Dinitrogen pentoxide	5	white solid very soluble water, decomposes in water

Nitrogen N_2 is an inert gas that exists in approximately 80% of the air humans breathe. However, a single atom of nitrogen (N) can be reactive and can exhibit ionisation states known as valence states from (+1 to +5). Hence, this allows nitrogen can form several oxides. The family of nitrogen oxide (NOx) compounds and their properties was shown in TABLE 2-1. The NO_x formation is a complex process that depends on various variables and mechanisms. The predominant nitrogen oxide is NO (90 - 95%) [38], followed by a small amount of NO_2 and other oxides of nitrogen species in very small quantities due to the combustion process. The nitrogen oxide formation from all combustion processes has three major mechanisms. These are thermal NO_x, fuel NO_x and prompt NO_x

2.2 Mechanism of NO_x formation in the combustion process

2.2.1 Thermal NO_x formation

Thermal NO_x formation is the process by which N_2 react with O_2 due to the combustion process to form NO_x. This reaction favours high temperatures, so hot spot areas that have higher temperatures than average areas produce a high amount of NO_x.

Moreover, the retention time and turbulence in the combustion chamber [39] are very important, affecting the NO_x formation. Generally, the formation of NO_x in this process primarily follows three equations expressed as R (2-1) and R (2-2) called "The Zeldovich mechanism"[40]. Initiate a nitrogen molecule (N_2) reaction with an oxygen atom to produce NO and a nitrogen atom R (2-1); this reaction insignificance is below 1800 K [41]. Then the nitrogen atom (N) further reacts with an oxygen molecule (O_2) to form an addition NO and O as shown in R (2-2).

$$N_2 + O \rightleftarrows NO + N \qquad \text{R (2-1)}$$

$$N + O_2 \rightleftarrows NO + O \qquad \text{R (2-2)}$$

The extended (or modified) Zeldovich mechanism adds a third elementary reaction R (2-3) to the original thermal NO mechanism.

$$N + OH \rightleftarrows NO + H \qquad \text{R (2-3)}$$

This reaction involves the interaction of atomic nitrogen and hydroxyl radicals from the combustion of existing water to nitric oxide formation.

2.2.2 Fuel NO_x

The pathway for fuel NO_x emissions arises from the oxidation of nitrogen-containing compounds inherently present in the fuel. The mechanism of fuel NO_x formation is complex and not yet fully understood. The overall reaction for the oxidation of fuel-bound nitrogen can be represented by R (2-4).

$$C_aH_bO_cN_dS_e + O_2 \rightarrow xNO + yH_2O + otherproduct \qquad \text{R (2-4)}$$

The fuel NO_x formation depends on the nitrogen content of the fuel and the combustion temperature [42]. Especially, coal combustion are the primary sources of fuel NO_x due to the high nitrogen content in the fuel [38,43].

2.2.3 Prompt NO_x

The classical prompt NO_x mechanism was proposed called by the "Fenimore pathway" after Fenimore discovered in 1971 [44]. which occurs in a flame front of combustion [45].This reaction involves the reaction between N_2 in the combustion air and hydrocarbon radicals such as CH and CH_2 to produce hydrogen cyanide (HCN) and atom nitrogen (N), as shown in R (2-5).

$$N_2 + CH \rightleftarrows HCN + N \qquad \text{R (2-5)}$$

Then HCN reacts with OH to form cyanide radicals (CN) molecule, after that the CN molecule reacts with oxygen to produce the NO, following (R (2-6)-R (2-7)):

$$HCN + OH \rightleftarrows CN + H_2O \qquad \text{R (2-6)}$$

$$CN + O_2 \rightleftarrows NO + CO \qquad \text{R (2-7)}$$

More advanced research presented that the formation of cyanonitrene radical (NCN) contributes to the NO formation pathway; this mechanism was presented by Moskaleva and Lin [35], shown in R (2-8).

$$N_2 + CH \rightarrow NCN + H \qquad \text{R (2-8)}$$

Then, the NCN radical can further lead to the NO formation following R (2-9) – R (2-11).

$$NCN + H \rightleftarrows HCN + N \qquad \text{R (2-9)}$$

$$NCN + O \rightleftarrows CN + NO \qquad \text{R (2-10)}$$

$$NCN + OH \rightleftarrows HCN + NO \qquad \text{R (2-11)}$$

Some studies utilise computational fluid dynamics (CFD) and chemical reaction networks (CRNs) to model the pathways. These models demonstrate that the interaction between various hydrocarbon radicals and molecular nitrogen leads to complex sequences involving intermediates such as NH and NCN, ultimately contributing to NO production under different conditions [39]. Moreover, the prompt NO_x formation was varied by type of fuel and combustion situation. Alessandro et al. [46] show that fuels with higher hydrocarbon content or those combusted at richer equivalence ratios exhibit more significant contributions $N_2O+O \rightleftarrows 2NO$ from the prompt NO_x mechanism.

2.2.4 NNH mechanism

The NNH mechanism involves the NNH radicals, which lead to the formation of NO. In this mechanism, N_2 react with hydrogen radicals H to form the NNH radical as an intermediate species. The subsequent interaction between NNH and atomic oxygen (O) produces NO and regenerates a hydrogen radical expressed in R (2-12)-R (2-13). This reaction was proposed by BOZZELLI and DEAN [47].

$$N_2 + H \rightleftarrows NNH \qquad \text{R (2-12)}$$

$$NNH + O \rightleftarrows NO + NH \qquad \text{R (2-13)}$$

Although less significant than thermal or prompt NO_x pathways, the NNH mechanism becomes relevant in hydrogen-rich flames and under low-pressure conditions [48].

2.2.5 N_2O pathway

The N_2O mechanism involves the formation of nitrous oxide (N_2O) as an intermediate, which then decomposes to produce NO shown in R (2-14).

$$N_2 + O + M \rightleftarrows N_2O + M \qquad \text{R (2-14)}$$

This pathway contributes to NO formation at moderate temperatures and high pressures, especially in lean combustion. Its contribution is generally smaller compared to thermal and prompt NO_x mechanisms [48]. Additionally, the lower temperatures typical of lean-fuel conditions suppress the thermal pathway. In such scenarios, the N_2O pathway becomes the primary route for NO production, particularly under high-pressure conditions where three-body reactions remain active due to the presence of a third molecule (M) [39].

2.3 Environmental and health impact from NO_x emissions

NO_x is among the most significant pollutants, mainly emitted by combustion. NO_x formation has several paths as expressed previously. Controlling NO_x emissions has become a critical focus within emission control due to their profound adverse impacts on human health, environmental systems, and global climate stability.

NO_x poses a significant risk to public health, as evidenced by a rise in hospital admissions [49]. Exposure to high concentrations of NO_x, particularly NO_2, has been associated with adverse effects on lung health. Research indicates that it can worsen symptoms of chronic respiratory conditions such as asthma and chronic obstructive pulmonary disease (COPD) [50]. Contact with NO_2 has been linked to reduced lung function, including decreased Forced Expiratory Volume (FEV_1) [51]. Even within existing air quality regulations, increasing NO_2 exposure before a respiratory virus infection is significantly linked to a higher number of subsequent asthma exacerbations [52]. In addition, research shows that children who are exposed to NO_2 significantly

suffer from asthma even though the concentration of NO_2 is under the standard of EPA [53].

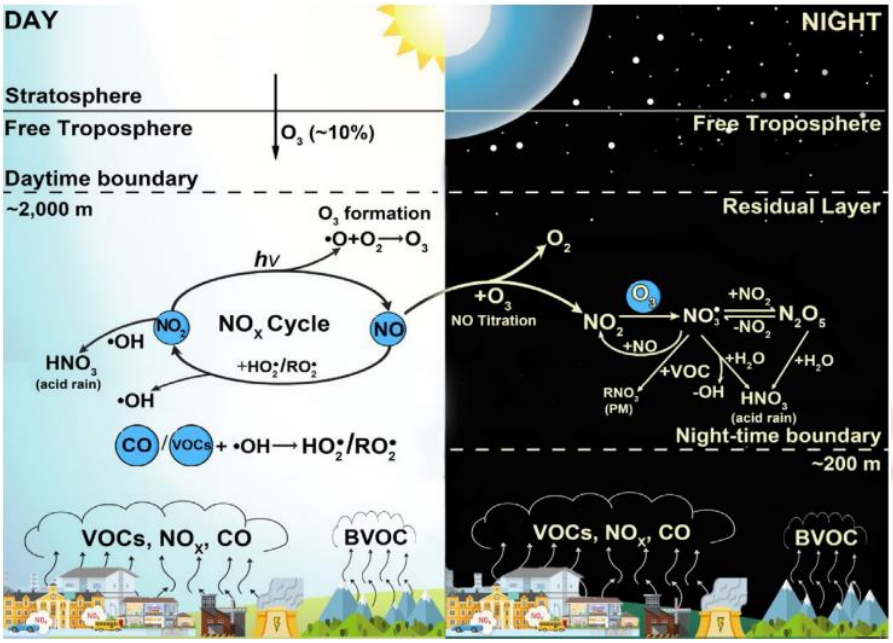

FIGURE 2-1 NO_x and ozone atmospheric during the day and night [54].

Furthermore, NO_x acts as a precursor, such as VOCs reacting with atmosphere sunlight to form ground-level ozone [55], as shown in FIGURE 2-1. Photochemical ozone production occurs predominantly during daylight hours, reaching its peak at midday due to maximum solar irradiation. As solar intensity decreases, ozone levels gradually decline. Subsequently, ozone concentrations in the atmosphere diminish at sunset due to NO titration, reaching their lowest levels late at night or early morning [56]. During nighttime, NO_2 undergoes oxidation by O_3, leading to nitrate radicals (NO_3) formation. These radicals subsequently react with VOCs to produce organic nitrate aerosols (RNO_3) [57]. In addition, these aerosols contribute to respiratory and cardiovascular health issues. Ozone, known for its harmful effects on human health, could cause pain in the respiratory system, eyes, nose, and throat, as well as exacerbate asthma attacks [52]. Recent research indicates the association between increased mortality rates from respiratory and cardiovascular disorders and the duration of exposure to ozone, even at concentrations below the existing regulatory levels [53]. Another indirect consequence of NO_x emissions is their role in forming particulate matter (PM2.5) [58], through atmospheric reactions with ammonia and other compounds. These fine particles can pass through deep into the human respiratory system, enter the bloodstream, and contribute to cardiovascular, neurological, and systemic health issues. Epidemiological studies consistently link high levels of NO_x pollution to increased hospitalisation rates, premature mortality, and a significant public health burden, particularly in densely populated urban regions.

2.4 The regulation of nitrogen oxides

NO_x is a direct and indirect effect that unpleasantly affects human health and furthers the environment, such as rain acid and exhibits as precursors to cause ozone

ground level. Moreover, the NO_x is also the cause of PM2.5. Hence, global NO_x emission regulations are increasingly stringent because of these health and environmental impacts, reflecting a commitment to reducing environmental and health impacts. Most countries regulate NO_x emissions from stationary sources (e.g., power plants and industrial boilers) as well as mobile sources including vehicles. This overview examines recent regulations in Thailand and the European Union (EU). The goal is to show how different nations set emission limits and identify trends towards stricter NO_x control.

In August 2023, Thailand's Ministry of Natural Resources and Environment issued two notifications establishing air-emission standards for power plants: (1) Notification defining standards for controlling air emissions from power plants, B.E. 2566 (2023), and (2) Notification designating power plants as sources of pollution. These regulations established differentiated standards for existing plants (licensed before the effective date) and new plants, with limits varying by fuel type and capacity of the plant. Old power plants have emission limits for gaseous pollutants (ppm) and particulate matter (mg/m^3). The new regulations allow lignite-fired units built before 1996 to emit up to 500 ppm NO_x. Coal-fired units licensed between 1996 and 2010 must comply with 350 ppm NO_x and 120 mg/m^3particulate limits. Plants using natural gas have more stringent requirements: $NO_x \leq 120$ ppm and $PM \leq 60$ mg/m^3. The NO_x limit for biomass and biogas-fired plants is 200 ppm, regardless of their capacity. Facilities permitted from 2010 to 2023 have lower particulate limits (≤ 80 mg/m^3) while maintaining NO_x limits of 200 ppm. Additionally, the 2023 notifications establish new, much stricter plant standards. With $PM \leq 30$ mg/m^3, new coal plants larger than 100 MW must reduce SO_2 to ≤ 20 ppm and NO_x to 120 ppm. The most stringent restrictions apply to natural gas plants, which need $NO_x < 80$ ppm and $PM < 20$ mg/m^3. Although particulate standards are stricter (≤ 90 mg/m^3 for biomass and ≤ 30 mg/m^3 for biogas), biomass and biogas plants might release up to 200 ppm NO_x. Waste-to-energy facilities are required to stick to NO_x limits of 150 ppm for new plants and 180 ppm for old plants. For coal-fired units, mercury limits of ≤ 0.03 mg/m^3 were set. These emission limits were summarised in TABLE 2-2.

TABLE 2-2 Emission limits of various power plant categories according to Thai environmental regulations. [59]

Power plant category	**Emission limit**		
	NO_x (ppm)	**SO_2 (ppm)**	**PM (mg/m^3)**
Old coal plants (1996–2010)	≤ 350	-	≤ 120
Old natural-gas plants	≤ 120	-	≤ 60
New coal plants > 100 MW	≤ 120	≤ 20	≤ 30
New natural-gas plants	≤ 80	-	≤ 20
New biomass/biogas plants	≤ 200	-	≤ 90 (biomass) or ≤ 30 (biogas)

The EU's Industrial Emissions Directive (IED) 2010/75/EU requires the use of best available techniques (BAT) and integrates pollution control throughout the EU. BAT conclusions for large combustion plants (LCP BREF), which introduced best available techniques-associated emission levels (BAT-AELs), were adopted via the EU in 2017. By 2021, existing plants (>300 MWth) must typically comply with these

emission ranges. The LCP BREF specifies the following BAT-AEL ranges for current power plants concerning NO_x emissions, which are summarised in TABLE 2-3.

TABLE 2-3 IED NO_x limit BAT-AELs for existing large combustion plants (> 300 MWth) [60]

Fuel/technology (>300 MWth)	**NO_x BAT-AEL (mg/Nm³)**	**Remark**
Coal – fluidised bed combustion (FBC)	150–175	Upper end applies to FBC boilers commissioned before 2014
Coal – pulverised combustion (PC)	150	Derogations possible for plants operating <1,500 h/year
Lignite – PC	150–175	Higher value applies to boilers commissioned before 2014
Biomass/peat	150 (≤160 mg/Nm³ if before-2014)	-

For all these categories, the prior IED emission limit value (ELV) for NO_x was 200 mg/Nm^3. For coal and lignite plants, the BREF lowers the permissible NO_x concentration by roughly 25%. The SO_2 BAT-AELs for lignite-fired and coal-fired pulverised plants were reduced to 130–200 mg/Nm^3. The BREF suggests a NO_x limit of 85 mg/Nm^3 for new coal and lignite plants, according to industry analyses compiled in the Institute for Energy Economics and Financial Analysis report [60]. Compared to the 150–175 mg/Nm^3 range for current units, this limit is much stricter.

To reduce dangerous exhaust pollutants from transportation, the European Union (EU) set a set of increasingly strict emission standards called the Euro standards. By lowering emissions of NO_x, HC, CO, and PM, these rules hope to improve air quality and advance national health and climate goals. Advances in vehicle and emission-control technology are reflected in each subsequent Euro stage, especially for diesel engines, which have historically released higher levels of NO_x. According to TABLE 2-4, the EU has maintained the 60 mg/km limit for gasoline-powered vehicles while significantly reducing the permitted NO_x emission limits for diesel passenger cars from 180 mg/km under Euro 5 to 80 mg/km under Euro 6. To provide a more thorough approach to real-world emission control. The EU introduced real-driving-emission tests via Commission Regulation 2016/646.

To bridge the gap between laboratory and road emissions, the regulation specifies two steps: an initial phase requiring a conformity factor of 2.1 (allowing NO_x emissions up to 2.1 × the 80 mg limit) and a second phase, 1 year and 4 months later, that requires full compliance with the $80\ \mathrm{mg \cdot km^{-1}}$ limit plus only a measurement-uncertainty margin. A 2015 Commission press release explains that Member-State representatives agreed that the discrepancy between laboratory and on-road emissions must fall to 2.1 for new models from September 2017 and to 1.5 for new models by January 2020 (January 2021 for all new vehicles) [61]. The subsequent Euro 7 regulation, which is anticipated to be implemented in 2025, keeps these NO_x levels but introduces more extensive durability and pollutant requirements, such as NH_3 and particle number limits.

TABLE 2-4 European Union (EU) Vehicle Emission Standards and NO_x Limits (Euro 5 – Euro 7)

Standard	Fuel Type	NO_x Limit (mg/km)	Remark	Ref
Euro 5 (2011)	Diesel	≤ 180	Introduced stricter NO_x limits for diesel vehicles; maintained 60 mg/km for petrol cars.	[62]
	Petrol	≤ 60	-	
Euro 6 (2015-2020)	Diesel	≤ 80	Introduced Real-Driving Emissions (RDE) tests allowing exceedances (conformity factors = 2.1 → 1.5); real-world emissions often 200–560 mg/km.	
	Petrol	≤ 60	Limit unchanged from Euro 5.	
Euro 7	Diesel	≤ 80	Extends durability to 160,000 km; adds NH_3 (ammonia) limits; tightens particle number emissions.	[63]
	Petrol	≤ 60	Same NO_x limit as Euro 6 but stricter durability and pollutant coverage.	

In summary, both Thailand and the European Union (EU) have progressively tightened NO_x emission standards in recent years. Thailand's 2023 notification lowered the allowable NO_x concentration for new coal-fired power plants from 200 ppm under the 2009 standard to 120 ppm, while introducing a stricter 80 ppm limit for natural-gas-fired units. Similarly, the EU's Best Available Techniques Reference Document (BREF) prescribes BAT-AELs of 150–175 mg/Nm^3 for existing large combustion plants and 85 mg/Nm^3 for new installations. Thailand's regulations differentiate by fuel type and plant age, setting looser limits for biomass and biogas plants (≤ 200 ppm), whereas the EU distinguishes between combustion technologies such as fluidised-bed and pulverised-coal systems, as well as by fuel category. Measurement conventions also differ: Thailand reports gaseous pollutants in ppm and particulates in mg/m^3, while the EU expresses all in mg/Nm^3, requiring careful conversion for comparison. Despite these tightening measures, implementation challenges remain—many older Thai lignite-fired units are still permitted up to 500 ppm NO_x, and practical compliance in both regions often lags behind formal standards.

2.5 Selective Catalytic Reduction (SCR)

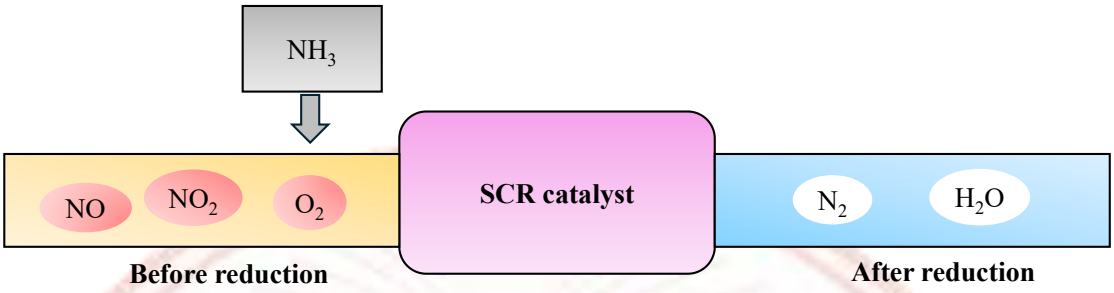

FIGURE 2-2 Selective catalytic reduction with NH_3 as a reductant

SCR is an emission control technology used to reduce NO_x from exhaust gases, primarily in industrial flue gas systems and diesel engine exhaust. The process involves injecting a reductant into the exhaust stream, typically ammonia (NH_3), urea, hydrocarbons (HC), hydrogen (H_2), and carbon monoxide (CO) to reduce NO_x [64]. The mixture then passes over a catalyst, which facilitates the reduction of NO_x into nitrogen (N_2) and water (H_2O). The NH_3-SCR process as shown in FIGURE 2-2, consists of essential chemical reactions, with the initial reaction recognised as the "Standard SCR" reaction R (2-15) and R (2-16). This reaction is defined by stoichiometry, which maintains an equal balance of NO and NH_3. On the other hand, reaction R (2-17) is referred to as the "Fast SCR" reaction, notable for its exceptional efficiency [64,65]. This technique has a high potential for reducing the environmental and health effects [66].

$$4NO + 4NH_3 + O_2 \rightarrow 4N_2 + 6H_2O \text{ (Standard SCR)} \qquad \text{R (2-15)}$$

$$2NO_2 + 4NH_3 + O_2 \rightarrow 3N_2 + 6H_2O \qquad \text{R (2-16)}$$

$$4NH_3 + 2NO + 2NO_2 \rightarrow 4N_2 + 6H_2O \text{ (Fast SCR)} \qquad \text{R (2-17)}$$

Commercial vanadium-based SCR catalysts typically operate within an optimal temperature range of 300–400°C, achieving $DeNO_x$ efficiencies exceeding 90% [67]. However, prolonged exposure to extreme conditions such as high temperature [68], high dust concentration [69], and high sulphur concentrations [70] these can lead to catalyst deactivation. subsequently reducing $DeNO_x$ efficiency and shortening catalyst lifespan. Furthermore, during startup, shutdown, or low-load operation of coal-fired boilers, the flue gas temperature may drop below the optimal range, further affecting the catalytic performance. Over the last decade, vanadium oxide catalysts supported on TiO_2 have been the predominant choice for SCR applications, achieving more than 90 % NO_x conversion efficiency at temperatures below 300 °C [71]. Despite their strong low-temperature performance, VO_x/TiO_2 catalysts suffer from reduced stability and catalytic activity at higher operating temperatures [72]. Hence, the challenge of the SCR is requiring the control system to control ammonia injection, preventing excess ammonia from the reaction process [73]. This method may face catalyst deactivation due to poisoning from sulphur, particulate matter, or heavy metals and ammonia slip.

2.6 Selective Non-Catalytic Reduction (SNCR)

Selective Non-Catalytic Reduction, or SNCR, constitutes a notable technology for the abatement of nitrogen oxides, specifically their conversion of NO_x into elemental nitrogen and water. A key characteristic of SNCR is the contradistinction to SCR operating in the absence of a catalyst. In this approach, inject NH_3, urea, and cyanuric acid as a reducing agent [74]. In opposition to Selective Catalytic Reduction (SCR), SNCR uses thermal reactions to promote NO_x reduction and operates at higher temperatures than SCR (usually between 800 and 1300 °C) [74]. The performance of the SNCR method is typically 50 – 75%. These include the prevailing temperature of the flue gas, the reducing agent selected for use, and the duration of the retention time for the reaction to proceed. Optimisation of these factors is therefore paramount in maximising the effectiveness of NO_x reduction achieved through the SNCR technique.

2.7 Mechanism of NO oxidation to NO_2 by O_3 generated from plasma

In plasma-based systems, ozone generation plays a crucial role in promoting the oxidation of NO into NO_2, which significantly enhances the overall effectiveness of SCR processes. Ozone quickly reacts with NO through a gas-phase oxidation process when it is added, producing NO_2 in a regulated way. The so-called "fast SCR" reaction pathway is facilitated by the presence of NO and NO_2 in a 1:1 molar ratio, which makes this transformation especially advantageous. For this reason, pre-oxidation of NO with ozone increases the SCR activity at low temperatures, which results in more effective NO_x removal, less ammonia slip.

The generated ozone then acts as a strong oxidising agent, readily reacting with NO to produce NO_2, as shown in R (2-18) [75]

$$NO + O_3 \rightarrow NO_2 + O_2 \qquad \text{R (2-18)}$$

This reaction mechanism forms the foundation for plasma-assisted NO oxidation. By coupling the plasma-generated ozone, the overall NO_x abatement performance can be significantly enhanced, enabling more efficient pollutant control of the SCR even under low-temperature flue gas conditions. Within plasma technology, energetic electrons collide with oxygen molecules, causing oxygen dissociation into a single atom of oxygen, as represented in R (2-19) – R (2-20) [76].

$$e + O_2 \rightarrow e + O(^3P) + O(^3P) \qquad \text{R (2-19)}$$

$$e + O_2 \rightarrow e + O(^3P) + O(^1D) \qquad \text{R (2-20)}$$

The resulting atomic oxygen species subsequently recombine with molecular oxygen through a three-body collision mechanism to form ozone in R (2-21).

$$O + O_2 + M \rightarrow O_3 + M \qquad \text{R (2-21)}$$

Where M stands for a third partner such as O, O_2 or N_2.

2.8 Plasma technology

Plasma is a quasi-neutral gas that follows the more commonly recognised states of solid, liquid, and gas. Plasma is essentially an ionised gas characterised by a chemically reactive medium containing a diverse range of species, including electrons, positive and negative ions, free radicals, and gas atoms and molecules in both their ground and excited states FIGURE 2-3. Plasma can exist across a broad spectrum of temperatures and pressures, and it can be generated under low-pressure or atmospheric-

pressure conditions. The formation of plasma involves the coupling of energy to a gaseous medium through various mechanisms, including mechanical, thermal, chemical, radiant, and nuclear processes, as well as through the application of voltage or the injection of electromagnetic waves. In many cases, a combination of these methods is employed to induce the dissociation of gas molecules, resulting in a complex mixture of ions, electrons, neutral gas molecules, and other reactive species. This highly energetic chemical environment enables a unique and diverse range of chemical reactions that are typically inaccessible in other states of matter.

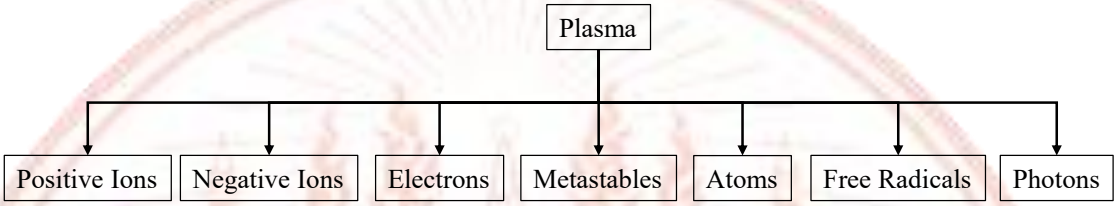

FIGURE 2-3 Constituents of plasma [77]

TABLE 2-5 Classification of plasma [77]

Plasma	State	Application
High temperature plasma (Equilibrium plasma)	$T_e \approx T_i \approx T_g = 10^6$ to 10^8 K $N_e \geq 10^{20}$ m^{-3}	Laser fusion plasma
Low-temperature plasma		
Thermal plasma (Quasi-equilibrium plasma)	$T_e \approx T_i \approx T_g \leq 2 \times 10^4$ K $N_e \geq 10^{20}$ m^{-3}	Arc plasma, plasma torches, RF inductively coupled discharges
Non-thermal plasma (Non-equilibrium plasma)	$T_e \gg T_i \approx T_g \leq 2 \times 10^4$ K $N_e \geq 10^{20}$ m^{-3}	Glow, corona, DBD, etc
T_e, T_i, and T_g represent the temperatures of the electrons, ions, and neutral gas species, respectively, while N_e denotes the electron density within the plasma.		

Plasmas are generally categorised into two principal types: high-temperature (fusion) plasmas and low-temperature (gas-discharge) plasmas, as summarised in TABLE 2-5. In high-temperature plasmas, all species electrons, ions, and neutral particles exist in thermal equilibrium, sharing nearly identical temperatures. Low-temperature plasmas, on the other hand, are further divided into thermal (quasi-equilibrium) and non-thermal (nonequilibrium or cold) types. Thermal plasmas exhibit near-equilibrium conditions among electrons, ions, and neutrals, and are typically generated using plasma torches or microwave devices. These systems produce intense heat fluxes, making them suitable for high-temperature applications such as material processing and waste treatment. However, in many technological fields, such extreme temperatures are unnecessary or even detrimental. In such cases, non-thermal or cold plasmas (NTP) are preferred. In cold plasmas, most of the input electrical energy is transferred to electrons, generating highly energetic electrons while keeping ions and neutral species near ambient temperature. This property allows cold plasmas to facilitate low-temperature plasma chemistry. Their unique combination of strong thermodynamic nonequilibrium, low gas temperature, and high concentrations of reactive species provides exceptional selectivity and versatility, enabling their use across a wide spectrum of scientific and

industrial applications [77].Owing to these characteristics, NTP is particularly well suited for ozone generation, where efficient oxidation reactions can occur without excessive thermal decomposition.

The role of plasma reaction with gas and change the state of gas was reported by [77] , fast electrons collide with rare-gas atoms and give them extra energy, causing them to become excited gas atoms or even ionised. These processes are shown in R (2-22)–R (2-24).

$$e + RG \rightarrow e + RG^{+} \quad \text{R (2-22)}$$

$$e + RG \rightarrow 2e + RG^{+} \quad \text{R (2-23)}$$

$$e + RG \rightarrow e + RG^{*} \quad \text{R (2-24)}$$

Electrons can also break halogen molecules into single atoms and negative ions, as described in R (2-25).

$$e + X_2 \rightarrow X + X^{-} \quad \text{R (2-25)}$$

Once the rare-gas atoms are excited, they can momentarily attach to nearby atoms during collisions, forming temporary excited molecules such as RG_2^* or RGX^*. These short-lived molecules are created through three-body collisions or through recombination of positive and negative ions, as shown in R (2-26)–R (2-29).

$$RG^{*} + RG + M \rightarrow RG_2^{*} + M \quad \text{R (2-26)}$$

$$e + RG_2^{+} \rightarrow RG_2^{*} \quad \text{R (2-27)}$$

$$RG^{+} + X^{-} + M \rightarrow RGX^{*} + M \quad \text{R (2-28)}$$

$$RG^{*} + X_2 \rightarrow RGX^{*} + X \quad \text{R (2-29)}$$

Because these molecules cannot exist in a stable, low-energy form, they quickly lose their excess energy and fall apart, releasing UV or VUV light in the process R (2-30)–R (2-31).

$$RG_2^{*} \rightarrow 2RG + hv \quad \text{R (2-30)}$$

$$RGX^{*} \rightarrow RG + X + hv \quad \text{R (2-31)}$$

In simple terms, the plasma first creates excited gas atoms, then these atoms briefly recombine, and finally they break apart while emitting ultraviolet radiation, which appears as the purple glow in the plasma region.

2.9 Type of plasma reactor

2.9.1 Corona discharge

In corona plasma, the electron temperature is significantly higher than that of ions and neutral molecules, resulting in strong thermal non-equilibrium and hence the classification as NTP. Excitation and recombination of charged and neutral species generate ultraviolet radiation and give rise to the characteristic faint blue violet glow of the corona, often accompanied by a subtle hissing or crackling sound A common configuration for generating corona discharge is the point plane arrangement, in which a high voltage is applied to a sharp needle electrode positioned above a grounded flat plate, as shown in FIGURE 2-4. The strong curvature at the needle tip produces an intense, highly non-uniform electric field, resulting in field enhancement that initiates electron avalanches once the corona onset voltage is exceeded. This creates a thin ionisation zone called the corona region in which energetic electrons, ions, and reactive species are formed through electron-impact dissociation of O_2 and H_2O, as widely reported in corona discharge studies [78]. Beyond this ionisation zone lies the drift

region, where ions and charged particles migrate toward the plane electrode under the influence of the weaker electric field. The point plane geometry provides a simple, stable, and controllable configuration for generating NTP, and is frequently used in research on NO oxidation and ozone production mechanisms. For example, Zhu et al. [79] employed a similar pointed electrode configuration to examine polarity-dependent corona behaviour and ozone distribution in the discharge region, while Molchanov et al [80]. demonstrated the role of corona-generated species in converting NO to NO_2 within small-scale combustion exhaust.

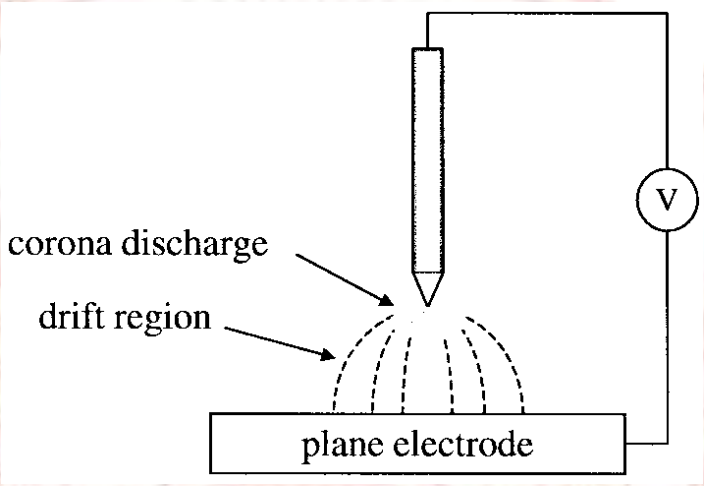

FIGURE 2-4 Corona discharge [78]

2.9.2 Microwave Discharge Plasma

Microwave discharges are electrodeless plasmas sustained by electromagnetic waves, typically at 2.45 GHz, enabling stable operation from 10.5 Torr to atmospheric pressure [81]. Their high electron power, coupling up to 90% absorption of incident microwave energy produces strongly nonequilibrium conditions that support efficient vibrational excitation and molecular activation [81]. The absence of electrodes prevents erosion and allows the plasma structure to be tuned through the design of the waveguide or resonant cavity, while their vibrationally driven chemistry is especially favourable for CO_2 and gas-phase reaction pathways [81]. Microwave plasmas are used in plasma chemistry, analytical diagnostics, thin-film processing, environmental treatment, and high-speed aerodynamics, where focused microwave plasmas serve as compact energy-deposition sources for supersonic and hypersonic flow control [82]. Recent studies highlight their effectiveness for CO_2 conversion. Plasma-catalytic configurations using NiO/TiO_2 significantly increase conversion and energy efficiency relative to plasma-only operation due to plasma-generated oxygen vacancies and enhanced dissociative electron attachment [83]. Supersonic microwave reactors achieve the highest reported energy efficiencies (up to ~90 %), although conversion remains modest (≈10–28 %), reflecting a fundamental trade-off between energy cost and single-pass conversion [83]. Focused microwave discharges can generate one to four plasmas, with gas temperatures rising to ~410–452 K within microseconds, governed first by excited-state quenching and later by vibrational–translational relaxation [82]. Overall, microwave plasmas offer highly efficient non-thermal energy transfer and scalable design, making them strong

candidates for plasma-assisted gas conversion, catalytic activation, and advanced flow-control applications.

2.9.3 Gliding Arc Discharge Plasma

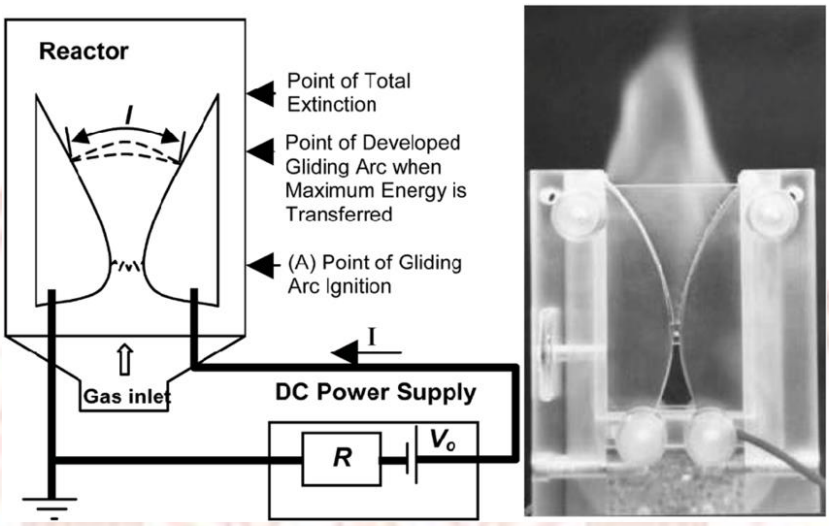

FIGURE 2-5 Gliding arc reactor [84]

Gliding-arc (GA) plasmas belong to the class of "warm" non-thermal plasmas, characterised by gas temperatures of roughly 1000–4000 K while maintaining electron energies sufficient for strong vibrational and electronic excitation of molecules [85]. A gliding arc (GA) reactor operates using two diverging electrodes placed in a flowing gas stream, shown in FIGURE 2-5, creating a discharge that transitions from a high-temperature arc to a stretched intermediate-temperature plasma as it "glides" along the electrodes. The arc is first ignited at the shortest electrode gap the point of highest electric field strength when the breakdown field in air reaches approximately 3 kV/mm. Immediately after ignition, the current rises rapidly while the voltage drops, forming a stable arc column. In rotating gliding-arc (RGA) reactors, two characteristic operating modes are typically observed: a rotating, short-residence-time arc (Mode I), and a longer, steady arc (Mode II) that reaches temperatures up to ~2600 K and residence times of ~10 ms, conditions under which vibrational–translational (VT) relaxation controls the chemistry [86]. The interaction between arc dynamics, flow structure, and reactive chemistry has been investigated extensively through multi-physics modelling studies. These show that a strong inlet vortex and a stable recirculation zone near the arc root extend the effective residence time up to ~17 ms and concentrate chemical activity within high-power-density regions close to the cathode pin and anode wall [87]. Other research development has led to reverse-vortex "plasmatron" geometries, which create a more volumetric discharge, enhance gas–plasma contact, and improve robustness for industrial processing [88]. Design guidelines emphasise maintaining the reduced electric field above ~3 Td in the active zone and limiting arc current to keep the discharge in the desired non-equilibrium regime [88]. Advances in diagnostics further support GA optimisation. Optically accessible 2D GA reactors, using combined high-speed imaging and optical emission spectroscopy, reveal detailed arc ignition, gliding, stretch, and extinction behaviour

under various feed gases such as H_2/Ar and different AC powers [89]. These studies show that arc stability and length are highly sensitive to gas composition and power density, providing practical insights for energy-intensive processes and plasma-assisted electrification strategies in applications such as CO_2 and CH_4 reforming.

2.9.4 Dielectric-Barrier Discharge (DBD)

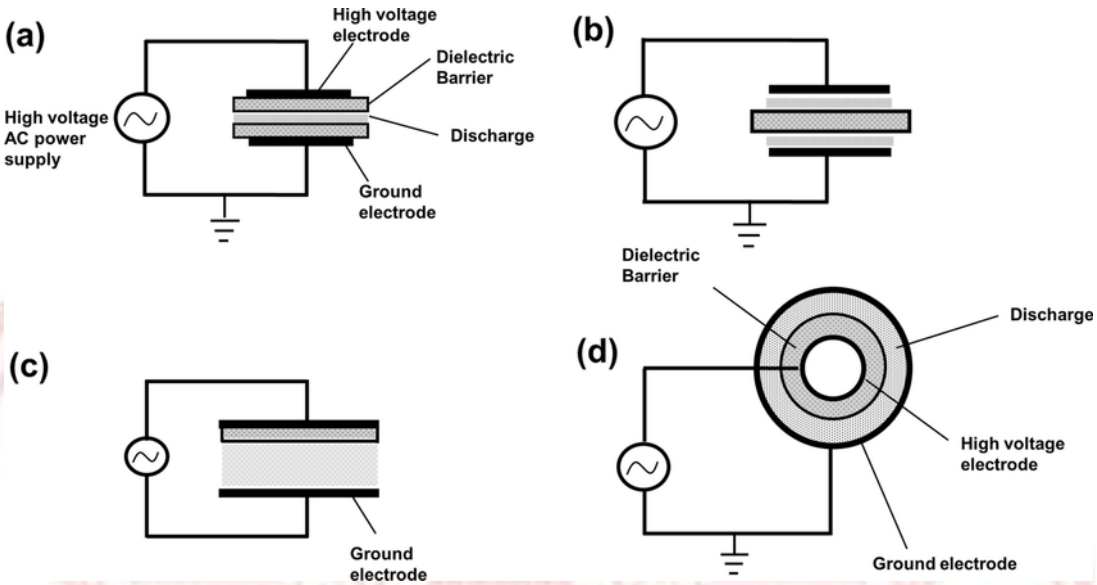

FIGURE 2-6 Typical configurations of dielectric barrier discharge (DBD) plasma reactors: (a) planar double DBD, (b) planar mid-barrier DBD, (c) planar half DBD, (d) cylindrical DBD.

Dielectric Barrier Discharge (DBD) is a type of non-thermal plasma generated between two electrodes separated by at least one dielectric layer. When an alternating high voltage is applied, numerous microdischarges form across the gas gap, producing energetic electrons without significantly heating the gas. This allows chemical reactions to occur efficiently at near-ambient temperatures, making DBD systems widely used for applications such as ozone generation [90]. FIGURE 2-6 illustrates several typical configurations of DBD plasma reactors used. In these systems, one or more dielectric layers are inserted between the metallic electrodes to enable stable discharge operation. The dielectric may cover either one or both electrodes, or it may be positioned between them without direct contact. When both electrodes are coated with dielectric material, as shown in FIGURE 2-6 (a), The configuration is referred to as a full dielectric barrier discharge, whereas covering only one electrode corresponds to a half dielectric barrier discharge FIGURE 2-6 (b). Direct plasma–electrode interaction can cause sputtering and chemical corrosion, leading to the introduction of impurities into the plasma; thus, the full DBD arrangement is preferred when high-purity plasma generation is required. The cylindrical DBD configuration (FIGURE 2-6 (d)) consists of a central high-voltage electrode surrounded coaxially by an outer grounded electrode, with at least one dielectric tube separating them [91].

DBD has long been recognised as one of the most practical and energy-efficient plasma technologies for generating ozone at atmospheric pressure, owing to its inherent ability to limit current, prevent arcing, and sustain large volumes of non-thermal

plasma. In DBD reactors, electrons are energetically hot while the bulk gas remains comparatively cold, enabling dissociation of O_2 into O-atoms without excessive gas heating. This is essential for ozone synthesis, because elevated temperatures accelerate O_3 decomposition and drastically reduce yield. As shown in recent comparative work, glow-mode DBD maintains discharge-channel temperatures as low as ~305 K, resulting in markedly higher ozone yields of 342.6 g/kWh compared with streamer-dominated discharge, which can heat channels to 440–465 K and limit yield to ~162.6 g/kWh [92]. Ozone performance is sensitive to several intertwined reactor variables, including discharge mode, electric-field distribution, dielectric material, surface conductivity, and gap width. Studies have emphasised that narrow gaps (≈ 100–300 μm) significantly intensify the electric field, suppress low-energy electrons, and thus enhance ozone formation in O_2-fed reactors. Increasing gas pressure in narrow-gap systems further accelerates the three-body $O + O_2 + M \rightarrow O_3 + M$ process, improving ozone yield and equilibrium concentration [20]. Nevertheless, narrow gaps and high field strengths increase the risk of parasitic discharges at electrode–dielectric boundaries, which waste input energy and reduce effective ozone-production efficiency. The use of conductive coatings such as CrO_3, ZnO, or Ag layers has been shown to enhance surface conductivity, suppress partial discharge, and improve stability and uniformity of the plasma [20]. Notably, the silver-layer DBD (SL-DBD) design demonstrates how modifying electrode–dielectric interfaces can achieve stable hybrid discharge, alternating between streamer and glow-corona forms. This hybrid behaviour increases discharge intensity by up to fiftyfold and raises the O-atom emission peak at 777 nm to nearly 29,000 counts compared with ~18,000 in a standard streamer-only DBD reactor [93]. Sustained operation also reveals its robustness: ozone concentration remains stable at ~150 g/m^3 during an 8-hour continuous run, significantly outperforming a comparable reactor lacking the silver layer [93]. Beyond ozone generation itself, a growing body of research recognises the relevance of plasma-generated ozone for downstream NO_x control. In oxygen-rich or air-fed DBD reactors, NO and NO_2 can form and interact with O_3 in complex ways. High specific-energy input promotes not only O_2 dissociation but also N_2 excitation and dissociation, yielding NO that catalytically decomposes ozone at high ozone densities, a phenomenon often termed “ozone poisoning [20].

2.10 Flue gas volume flow rate measurement

Accurate measurement of flue-gas volumetric flow rate is essential for quantifying pollutant emissions, energy efficiency, and validating the mass balance in combustion systems. However, this measurement presents significant challenges due to the harsh exhaust environment. Flue gases often exhibit high temperatures ranging from about 150 °C in industrial boilers to over 700 °C in engine exhausts, which can degrade or damage conventional flow sensors [94,95]. In addition, the presence of condensable water vapour, corrosive species, and PM can cause sensor blocking, corrosion, and signal drift, resulting in large measurement uncertainties [96]. These factors make conventional techniques such as hot-wire anemometry, Pitot tubes, and thermal mass or ultrasonic flow meters unsuitable for long-term or high-temperature applications. Therefore, developing a reliable and robust approach for determining the flue-gas volume flow rate is challenging.

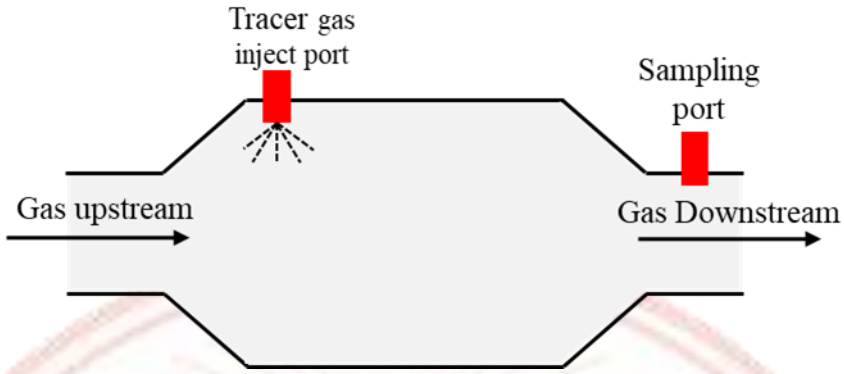

FIGURE 2-7 Concept of the tracer gas method

The tracer gas method is a volumetric measurement technique based on the principle of dilution, where a known quantity of tracer gas is introduced into a gas stream, and the resulting dilution is quantitatively assessed downstream, as shown in FIGURE 2-7. An ideal tracer gas should not naturally occur in the environment under investigation, thereby minimising background interference; commonly used gases include helium (He), sulphur hexafluoride (SF_6) [33], nitrous oxide (N_2O), and hexafluorobenzene (C_6F_6). Desirable characteristics of tracer gases include detectability at low concentrations, non-toxicity, non-allergenicity, chemical inertness, non-flammability, environmental safety for use in occupied spaces, and cost-effectiveness [34,97]. Notably, the tracer gas method is resilient to certain limitations that affect other flow measurement techniques; it is not constrained by non-uniform flow conditions, asymmetries in velocity profiles, or off-axis components induced by swirl. Furthermore, it does not require prior determination of the duct's cross-sectional area or the presence of a fully developed flow profile, nor does it necessitate a long duct length [26]. The method can be operationalised through four primary strategies of tracer gas injection: constant flow rate injection, pulse injection, concentration decay, and constant concentration techniques [35]. Historically, the tracer gas method has been applied to evaluate air leakage and heat loss in ventilation and HVAC systems [98,99], and in automotive contexts for quantifying the volumetric flow rate of exhaust gases [100,101]. In a notable study, Bryant [36] employed the tracer gas dilution method to calibrate flue gas flow in a large-scale calorimetry system. The findings revealed that this approach effectively calibrated averaging Pitot probes in exhaust ducts, reducing flow measurement bias by up to 6%. The literature indicates that the tracer gas dilution method offers significant advantages over conventional measurement techniques, underscoring its potential as a highly accurate alternative for volumetric flow rate determinations in flue gas systems.

Tracer-gas methods determine gas flow rate in ducts by introducing a known quantity of an inert tracer and measuring its concentration downstream. The relationship between tracer injection, tracer concentration, and a gas flow rate follows a conservation-of-mass formulation. For a well-mixed control volume, the general tracer mass-balance equation is shown in Eq. (2-1)

$$V\frac{dC(t)}{dt} = q_t C_e + F(t)C_e - F(t)C(t) \qquad \text{Eq. (2-1)}$$

Where V is the duct volume (m^3), $F(t)$ is the airflow rate through the duct (m^3/h), $q_t(t)$ is the tracer-gas injection rate (m^3/h), C_e is the tracer concentration in the injected

gas, and $C(t)$ is the tracer concentration in the duct at time t. The left-hand side represents the rate of change in concentration of tracer in the duct. The right-hand side accounts for tracer entering with the injection flow and upstream airflow, and tracer leaving with the duct flow. Different tracer-gas techniques arise from how the injection is controlled and how the concentration is measured.

There are four method that commonly use such as constant injection, pulse injection, concentration decay, and constant injection [35]. In constant injection method, a steady tracer flow is injected until the duct concentration reaches equilibrium ($dC/dt = 0$). With no tracer upstream ($C_e = 0$), Eq. (2-1) reduces to:

$$F(t) = \frac{q_t(t)}{C(t)} \qquad \text{Eq. (2-2)}$$

This method is widely used due to its simplicity and direct relationship between concentration and flowrate.

For the pulse-injection method, a short pulse of tracer is injected, after which no further tracer is added ($q_t = 0$). Substituting into Eq. (2-1) gives Eq. (2-3), and solving the resulting first-order differential equation yields Eq. (2-4):

$$V\frac{dC(t)}{dt} = -F(t)C(t) \qquad \text{Eq. (2-3)}$$

$$C(t) = C_0 e^{-F(t)/V} \qquad \text{Eq. (2-4)}$$

In the concentration-decay method, the behaviour is similar to the pulse-injection approach. After the tracer injection is stopped, the tracer concentration decreases naturally as it is carried out of the duct. The decay of $C(t)$ follows the same exponential form as in Eq. (2-4), and the airflow rate F is obtained from the decay constant.

Finally, in the constant-concentration method, the tracer-gas concentration in the duct is maintained at a specified setpoint by continuously adjusting the injection rate. Under steady-state conditions ($dC/dt = 0$) and assuming no tracer upstream, substituting into Eq. (2-1) yields:

$$F(t) = \frac{q_t(t)}{C(t)} \qquad \text{Eq. (2-5)}$$

CHAPTER 3
METHODOLOY

This chapter describes the experimental setup, instrument, and methodologies adopted in this research. The experiment was divided into three main parts. First, the inverted tracer-gas method was developed and employed to quantify the volumetric flow rate of simulated and real flue gases with high accuracy. This measurement is essential for validating the mass balance in subsequent experiments. Second, the DBD–NTP ozone generation system was constructed and characterised under various operating parameters to determine its electrical and chemical reactions, including ozone yield, production rate, and energy efficiency, as well as to investigate the formation of NO_x species during ozone generation. Third, the DBD–NTP reactor was applied for the treatment of NO_x in real flue gas, to evaluate the effectiveness of ozone-assisted NO oxidation under realistic flue gas conditions. The instruments, analytical equipment, and data acquisition systems used throughout the experiments are detailed to clarify their respective roles in system operation and monitoring. Finally, the procedures for data processing and analysis are presented.

3.1 Inverted tracer gas method setup

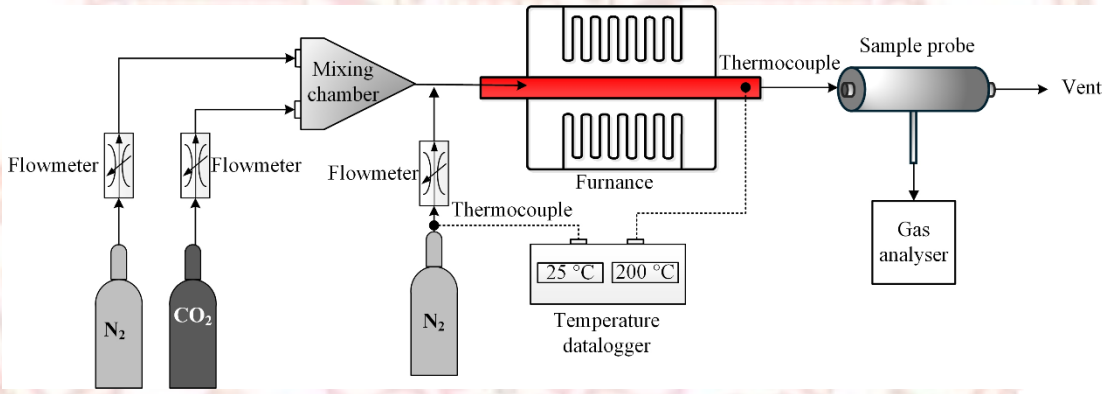

FIGURE 3-1 The schematic diagram of the inverted tracer gas method for proving the concept.

To prove the concept of the inverted tracer gas method for calculating gas volume flow rate in CHAPTER 4, A simulation of the flue gas stream was conducted on a laboratory scale to verify the gas flow characteristics, as illustrated in FIGURE 3-1. The simulated system consisted of a stainless-steel tube with an inner diameter of 0.5 inch and a total length of 1 m. To minimise heat loss during operation, the tube was insulated with ceramic fibre and installed within a furnace (operating range 30–3000 °C), which provided uniform heating to replicate the thermal environment of a real flue-gas stream. The gas temperature within the tube and the tracer-gas N_2 temperature were monitored using Type K thermocouples, with temperature data continuously recorded by a data logger. The simulated flue gas comprised a controlled mixture of CO_2 and N_2, blended in a gas-mixing unit. An additional N_2 stream was introduced downstream of the mixer as a tracer gas for flow-rate verification. The flow rates of both CO_2 and N_2 were regulated by mass-flow meters (model MF5706-N-10) to achieve the desired gas-flow conditions. The CO_2 concentration downstream of the furnace was measured using a

Testo 350 gas analyser, and the data were subsequently employed to determine the total volumetric flow rate using the inverted tracer-gas method.

3.2 Inverted tracer gas volumetric flow rate calculation

Nitrogen was selected as the inverted tracer because it remains chemically inert at flue-gas temperatures below 300 °C. At the same time, CO_2 was used as the indicator gas due to its high stability and ease of measurement. This method is based on the ideal gas law and the principle of molar conservation for CO_2 before and after dilution with N_2, assuming that the molar flow rate of CO_2 remains constant. Therefore, the molar flow balance can be expressed as Eq.(3-1).

$$\dot{n}_{CO_{2,0}} = \dot{n}_{CO_{2,1}} \quad \text{Eq. (3-1)}$$

where $\dot{n}_{CO_{2,0}}$ and $\dot{n}_{CO_{2,1}}$ denote the molar flow rates of CO_2 before and after dilution, respectively. The individual molar flow rates before and after dilution can be defined as shown in Eq. (3-2) and Eq. (3-3).

$$\dot{n}_{CO_{2,0}} = \dot{n}_f \times \%C_{CO_{2,0}} \quad \text{Eq. (3-2)}$$

$$\dot{n}_{CO_{2,1}} = (\dot{n}_f + \dot{n}_{N_2}) \times \%C_{CO_{2,1}} \quad \text{Eq. (3-3)}$$

where $\dot{n}_f$ is the flue-gas molar flow rate, $\dot{n}_{N_2}$ the tracer-gas molar flow rate, $\%C_{CO_{2,0}}$ is the CO_2 concentration before dilution, and $\%C_{CO_{2,1}}$ is the CO_2 concentration after dilution. Then, substituting Eq. (3-2) and (3-3) into Eq. (3-1), it becomes Eq. (3-4).

$$\dot{n}_f \times C_{CO_{2,0}} = (\dot{n}_f + \dot{n}_{N_2}) \times \%C_{CO_{2,1}} \quad \text{Eq. (3-4)}$$

Rearranging Eq. (3-4) for the molar flow rate of the flue gas:

$$\dot{n}_f = \dot{n}_{N_2} \times \frac{[\%CO_{2,1}]}{[\%CO_{2,0}] - [\%CO_{2,1}]} \quad \text{Eq. (3-5)}$$

The ideal-gas law is expressed as:

$$P\dot{V} = \dot{n}RT \quad \text{Eq. (3-6)}$$

where P is pressure, V is volume flow rate, n is the number of moles (mol), R is the ideal-gas constant, and T is temperature.

By differentiating Eq. (3-6) with respect to time, the molar flow rate becomes:

$$\dot{n} = \frac{P\dot{V}}{RT} \quad \text{Eq. (3-7)}$$

Substituting Eq. (3-7) into Eq. (3-5) gives:

$$\frac{P_f \dot{V}_f}{RT_f} = \frac{P_{N_2} \dot{V}_{N_2}}{RT_{N_2}} \times \frac{[\%CO_{2,1}]}{[\%CO_{2,0}] - [\%CO_{2,1}]} \quad \text{Eq. (3-8)}$$

Assuming that both the tracer gas and flue gas streams operate near atmospheric pressure and have negligible pressure difference ($P_f \approx P_t$), and Eq. (3-8) simplifies to:

$$\dot{V}_f = \dot{V}_{N_2} \times \frac{T_f}{T_{N_2}} \times \frac{[\%CO_{2,1}]}{[\%CO_{2,0}] - [\%CO_{2,1}]} \quad \text{Eq. (3-9)}$$

Eq. (3-9) provides the volumetric flow rate of the flue gas ($\dot{V}_f$), calculated from the known tracer-gas flow rate in this thesis use N_2 ($\dot{V}_{N_2}$), the measured concentrations of CO_2 before and after dilution ($\%C_{CO_{2,0}}$ and $\%C_{CO_{2,1}}$), and the corresponding gas

temperatures (T_f and T_{N_2}).This relationship forms the fundamental calculation basis for the inverted tracer-gas method used in both the laboratory and real-flue-gas experiments in this study.

3.3 DBD-NTP-generated ozone and simulated gas system.

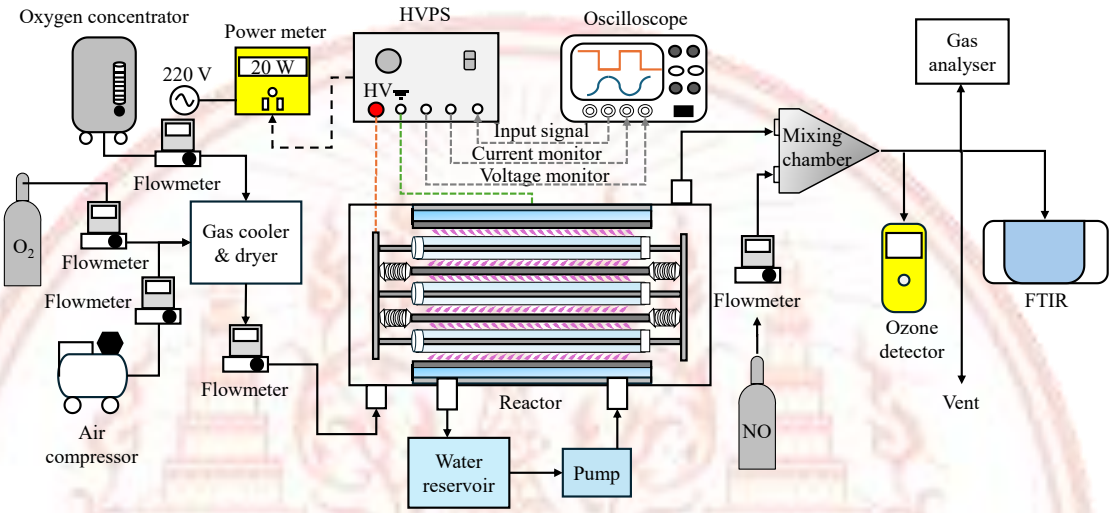

FIGURE 3-2 The schematic diagram of the DBD-NTP-generated ozone and simulated gas system.

The schematic diagram presented in FIGURE 3-2 illustrates the integrated configuration of the DBD-NTP ozone generation system and the simulated gas system employed in the experimental investigations of CHAPTER 5 and CHAPTER 6. The setup was designed to evaluate ozone generation performance under controlled laboratory conditions and to examine its subsequent application for NO oxidation. Compressed air provided the main feed, and ozone production was enhanced by adding high-purity oxygen (99.99 %-vol) delivered from either a cylinder or an oxygen concentrator. The mixed gas was passed through a cooler and dryer to remove heat and moisture prior to the DBD reactor, and the flow rate was controlled using a flow meter. The reactor was driven by a high-voltage power supply (HVPS) controlled and monitored using an oscilloscope to record discharge voltage and current waveform for power analysis. The discharge assembly was water-cooled through a circulating pump and reservoir to maintain thermal stability during continuous operation. The ozone-enriched gas produced at the DBD outlet was directed to a mixing chamber, where it is combined with a simulated gas stream containing NO from a gas bottle NO mixture in N_2 1000 ppm-vol. The mixed gases were then measured using a gas analyser and FTIR spectrometer to quantify NO_x production. The O_3 concentrations are also measured via ozone detector and FTIR. This configuration enabled accurate assessment of both ozone-generation characteristics and NO oxidation behaviour under well-defined flow, temperature, and composition conditions. The comparison of the DBD configuration of CHAPTER 5 and CHAPTER 6 are summarised in TABLE 3-1.

TABLE 3-1 Comparison of DBD reactor configurations used in CHAPTER 5 and CHAPTER 6

Parameter	Specification	
	CHAPTER 5	**CHAPTER 6**
Reactor material	Stainless steel	
Dielectric material	Quartz glass	Borosilicate glass
Number of discharge cell	single	Three
Outer diameter of dielectric glass (mm)	40	63
Length (mm)	500	
Discharge gap (mm)	0.5	1.15
Effective discharge volume (cm^3/cell)	34.43	5.42

3.4 Real flue gas with DBD-NTP system.

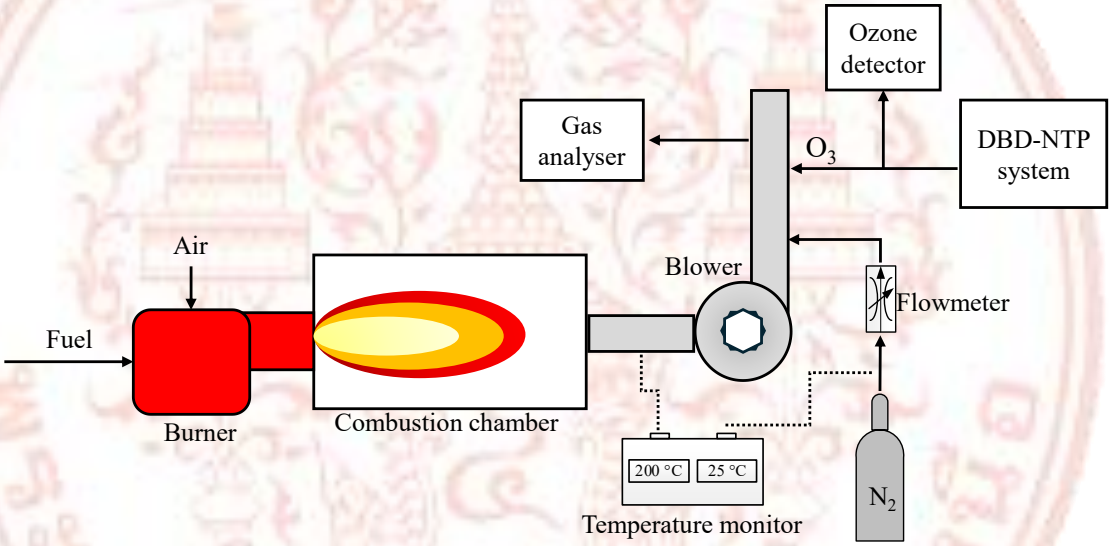

FIGURE 3-3 The schematic diagram of DBD-NTP generated ozone for treatment NO_x in real flue gas.

The experimental setup for the treatment of real flue gas, integrated with the DBD-NTP ozone generation system in CHAPTER 7, is illustrated in FIGURE 3-3. The schematic diagram was designed to evaluate the oxidation behaviour of NO to NO_2 in actual combustion exhaust gas. The diesel burner produced a steady flue-gas flow, which was directed to control the flow rate through a blower. The volume flow rate of the flue gas was determined by inverted tracer gas approach. The temperature of the upstream flue gas and the tracer gas were recorded via a thermocouple type K and a temperature datalogger (Picolog-TC08) for the calculated volume flow rate. Ozone generated from the DBD-NTP reactor was injected into the flue-gas stream upstream of the sampling point to ensure sufficient mixing and reaction with NO. Simultaneously, N_2 was introduced into the system at a desired flow inlet, which was controlled by a flow meter to determine the total volume flow rate of flue gas through the inverted tracer-gas technique. Gas composition was continuously monitored using a gas analyser and ozone detector located downstream of the DBD-NTP. These instruments provided real-time concentrations of NO, NO_2, and O_3, allowing for accurate evaluation of

ozone-induced NO oxidation efficiency. The integration of the inverted tracer-gas method ensured precise quantification of the flue-gas flow and residence time. These experiments discussed in CHAPTER 7, address the performance of the DBD-NTP system in real-flue-gas conditions and its potential application in industrial NO_x abatement processes. The configuration of DBD-NTP is brief in TABLE 3-2.

TABLE 3-2 Specifications of the DBD reactor used in CHAPTER 7

Parameter	Specification
Reactor material	Stainless steel
Dielectric material	Borosilicate glass
Number of discharge cells	12
Outer diameter of dielectric glass (mm)	23
Discharge gap (mm)	1.5
Effective discharge volume (cm^3/cell)	13.8

3.5 Instrument

3.5.1 Flue gas analyser

FIGURE 3-4 Testo 350 flue gas analyser

The Testo 350 combustion and emission analyser, as shown in FIGURE 3-4, employed to measure the concentrations of O_2, CO_2, NO, and NO_2 in both simulated and real flue-gas experiments. The instrument comprises a control unit and an analyser box containing electrochemical gas sensors, a gas pump, filters, and a condensate trap. It provides measurement ranges of 0–25 %-vol. for O_2, 0 to10 000 ppm for CO, 0–4000 ppm for NO, 0–500 ppm for NO_2, and up to 25 %-vol. for CO_2 (IR-based), with typical response times below 40 s. During the experiment, data is collected more than 3 times to ensure consistency of the results.

3.5.2 Ozone detector

To measure the ozone concentration generated by the DBD reactor, a customised SKZ-1050-O_3 analyser was employed as shown in FIGURE 3-5. The instrument is a CE-certified electrochemical gas analyser capable of detecting ozone concentrations within the range of 0–5000 ppm-vol with a resolution of 0.01 ppm and a response time of less than 10 s. The analyser continuously monitored ozone levels downstream of the reactor, allowing for real-time evaluation of plasma-generated ozone.

FIGURE 3-5 ozone detector SKZ-1050-O_3

3.5.3 Fourier Transform Infrared Spectroscopy (FTIR)

The FTIR spectrometer employed in this study was a Bruker INVENIO-R model (FIGURE 3-6), which operates based on the principle of infrared absorption spectroscopy. Each gas molecule possesses a distinct infrared absorption fingerprint arising from its characteristic vibrational and rotational energy transitions. By comparing the measured spectra of unknown gas samples with the reference spectra of known gases, the FTIR enables accurate identification and quantification of chemical species. In this study, the FTIR was used to continuously monitor the concentrations of O_3, NO, NO_2, N_2O, N_2O_5 and other gases produced during plasma discharge. The data were processed using OPUS software, where baseline correction and integrated absorbance calculations were performed for quantitative analysis.

FIGURE 3-6 Bruker INVENIO R

3.5.4 Waveform generation and Amplification

The waveform used to drive the DBD reactor was generated using a function generator integrated within the experimental control system and observed in real time on a digital storage oscilloscope (DSO) (Keysight DSOX1204G), see in FIGURE 3-7. which was supplied to a high-voltage power supply (HVPS) (Trek 20/20C-HS) for amplification. The Trek 20/20C-HS (FIGURE 3-8) is a high-performance amplifier capable of producing an output voltage of ± 20 kV_{peak} with a slew rate of 800 V/μs and a maximum peak current of 60 mA. The amplified voltage and discharge current were recorded simultaneously using the DSO, which provides four input channels, a 200 MHz bandwidth, and a sampling rate of 2 GSa s^{-1}. Both signals were obtained directly from the monitor output terminals of the Trek 20/20C-HS amplifier, which provides scaled representations of the actual high-voltage output and the corresponding current delivered to the load.

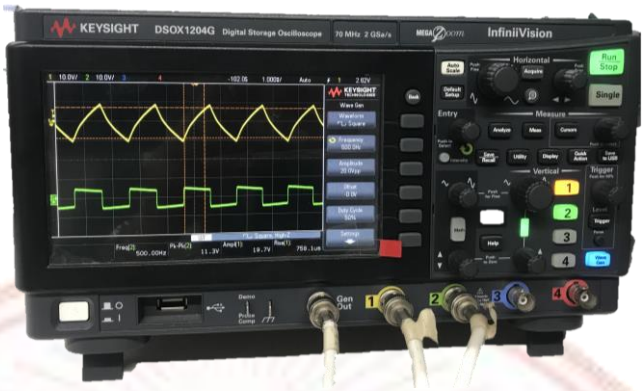

FIGURE 3-7 digital storage oscilloscope Keysight DSOX1204G

FIGURE 3-8 High voltage power supply (Trek 20/20C-HS)

3.6 Data processing

3.6.1 Discharge power

The discharge power **(P_D)** represents the actual electrical energy transferred from the high-voltage supply to the plasma during operation. It is a key parameter that determines the energy available for generating reactive species such as ozone and NO_2 in a DBD reactor. P_D was determined by integrating the instantaneous product of discharge voltage $V(t)$ and current $I(t)$ over one period of the applied waveform, then multiplying by the discharge frequency (f) or $1/T$ [102], as expressed in Eq. (3-10):

$$P_D = f \times \int_0^T I(t) \times V(t) dt = \frac{1}{T} \times \int_0^T I(t) \times V(t) dt \qquad \text{Eq. (3-10)}$$

3.6.2 Lissajous diagram (Q-V diagram)

The Lissajous diagram, which plots the charge (Q) against the discharge voltage (V). It provides insight into the energy transfer, discharge behaviour, and electrical characteristics of the plasma reactor. The Lissajous of the DBD requires simultaneous measurements of the reactor voltage and the corresponding charge. Traditionally, this is achieved by connecting a measurement capacitor in series with the reactor, where the Q is obtained as the product of the voltage across the capacitor and its capacitance. However, incorporating a physical measurement capacitor increases the overall capacitance of the reactor, potentially modifying its intrinsic electrical behaviour. To eliminate this influence, a virtual measurement capacitor was employed, and the charge was instead reconstructed by integrating the measured discharge current. Since the

oscilloscope records discrete data points, numerical integration was performed, and the accumulated charge is defined by Eq. (3-11) [103]

$$Q(t) = \sum_{i=1}^{N} I(t_i)\Delta t \qquad \text{Eq. (3-11)}$$

where $I(t_i)$ is the discharge current at a given time (t_i), $\Delta t$is the sampling interval, and N represents the total number of sampled data points.

3.6.3 Ozone production efficiency

The ozone production efficiency (OPE, μg/J), defined in Eq. (3-12), quantifies the effectiveness of ozone generation based on the discharge power supplied to the DBD reactor. Conversely, the system ozone production efficiency (SOPE, μg/J), expressed in Eq. (3-13), evaluates the total energy utilisation efficiency of the entire system by accounting for the actual electrical power consumed by the HVPS $(P_m, Watt)$.

$$OPE = \frac{OPR}{P_D \times 3.6} \qquad \text{Eq. (3-12)}$$

$$SOPE = \frac{OPR}{P_m \times 3.6} \qquad \text{Eq. (3-13)}$$

The ozone production rate (OPR, g/min) represents the mass of ozone produced by the reactor per unit time and serves as a key indicator of the reactor's output capacity. It can be determined using Eq. (3-14):

$$OPR = C_{O_3} \times q \qquad \text{Eq. (3-14)}$$

where $C_{O_3}$is the ozone concentration (g/ L) and q is the volumetric flow rate of the feed source gas of the DBD reactor (LPM).

The specific energy input (SEI, J/L) is a key parameter that stands for the amount of electrical energy supplied to the discharge per unit volume of gas flow rate. It provides a direct correlation between the electrical energy density and the resulting ozone production. The SEI can be calculated using Eq. (3-15):

$$SEI = \frac{P_D}{q} \times 60 \qquad \text{Eq. (3-15)}$$

Similarly, the specific overall energy input (SOEI, J/L) considers the total electrical energy drawn by the HVPS, thus reflecting the overall energy density applied to the system. It is defined as:

$$SOEI = \frac{P_m}{q} \times 60 \qquad \text{Eq. (3-16)}$$

The SEI and SOEI parameters are complementary to OPE and SOPE, respectively. They serve as the energy input counterparts to the ozone yield parameters, allowing for performance comparisons across different reactor configurations, discharge frequencies, and feed gas conditions.

CHAPTER 4
THE INVERTED TRACER GAS METHOD

This chapter presents an accurate determination of the volumetric flow rate of flue gas is essential, as it directly influences the estimation of pollutant emissions and the interpretation of removal efficiency. However, conventional flow measurement techniques are often hindered by the harsh conditions typical of flue gases, which include elevated temperatures, high moisture content, particulate matter, and chemically reactive species. These factors can compromise sensor performance and the accuracy of flow determination. The inverted tracer gas method was employed to address these challenges and is presented first in this chapter. When compared to the conventional tracer gas dilution technique, this method offers improved resilience to back pressure and environmental interferences, making it more suitable for application under realistic flue gas conditions. The results obtained demonstrate the reliability and practicality of this approach in determining flow rates for subsequent plasma experiments.

4.1 Preliminary laboratory scale at room temperature conditions

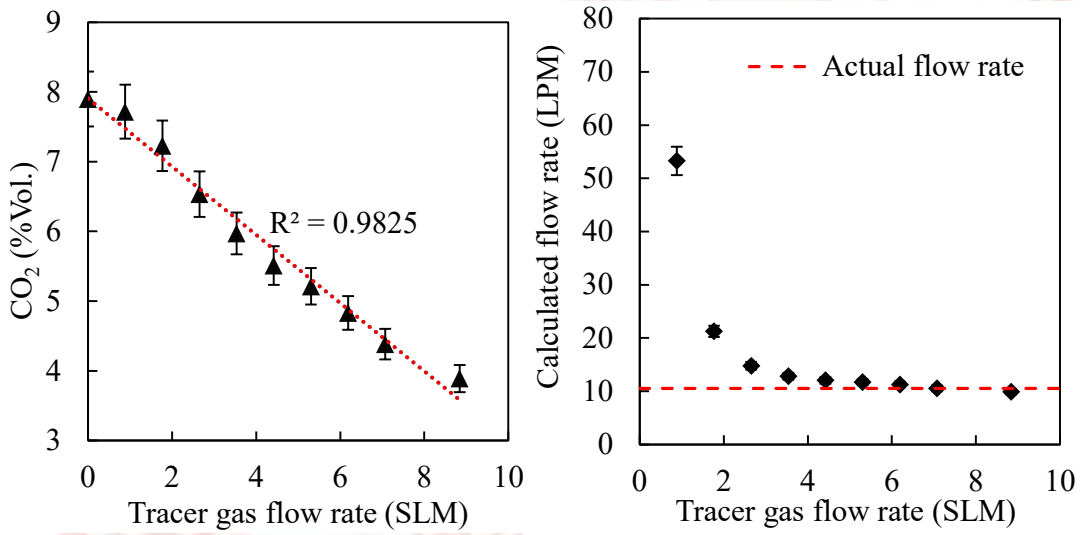

FIGURE 4-1 The effect of tracer gas flow rate on CO_2 concentration (left) and calculated original simulated flue gas flow rate (SLM) (right) at room temperature.

A preliminary laboratory experiment was conducted to validate the feasibility of the inverted tracer gas method for measuring the flue gas volume flow rate under controlled conditions. The experiment is in a laboratory setting where the ambient temperature is consistently maintained at approximately 25 °C using an air conditioning system to ensure environmental stability. The gas simulation system was initially calibrated using CO_2 and N_2, introduced at flow rates of approximately 1 SLM and 9 SLM, respectively, to replicate typical flue gas compositions. As illustrated in FIGURE 4-1 (left), the initial concentration of CO_2 was measured at approximately 8 %-Vol. Upon the gradual introduction of N_2, which acted as the tracer gas, the CO_2 concentration decreased steadily to slightly below 4 %-Vol. as the N_2 flow rate

increased from 1 to 10 SLM. This dilution behaviour corresponded well with the theoretical dilution effect. The experimental data showed a strong linear correlation, with a coefficient of determination (R^2) of 0.9825, indicating high consistency and minimal variability. The total volumetric flow rate of the simulated flue gas was subsequently calculated using the inverted method, as depicted in FIGURE 4-1 (right). These results confirm the validity and reliability of the proposed methodology under laboratory conditions, which is observed by a fixed 5% error bar on both figures.

4.2 Preliminary laboratory scale at elevated temperature conditions

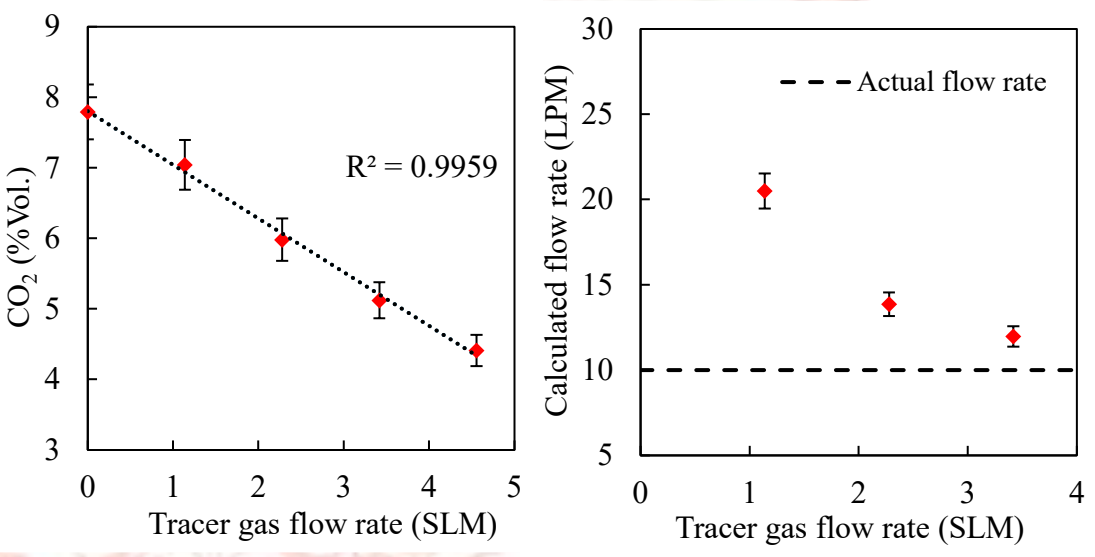

FIGURE 4-2 The effect of tracer gas flow rate on CO_2 concentration (left) and calculated original simulated flue gas flow rate (right) at 210 ± 10°C.

Following the initial proof-of-concept experiment, the simulated flue-gas system was maintained under the same operational conditions described in the preceding section. To evaluate the influence of temperature on the accuracy of the flow-rate calculation, the simulated flue-gas stream was subsequently heated using an oven to approximately 210 ± 10 °C, representing the typical thermal condition of exhaust gases downstream of emission after-treatment systems.

As show in FIGURE 4-2 (left) revealed the relationship between CO_2 concentration and tracer gas flow rate, where a gradual decrease in CO_2 concentration is observed with increasing tracer gas flow. The coefficient of determination (R^2 = 0.9959) indicates a strong linear correlation between the variables. Similarly, FIGURE 4-2 (right) illustrates the volumetric flow rate calculated using the inverted tracer gas method as a function of tracer gas flow rate. At higher tracer gas flow rates, the calculated flow rates demonstrate convergence, consistent with the results obtained at room temperature. These findings suggest that elevated temperature does not significantly affect the gas dilution process. These results indicate that elevated temperature does not significantly affect the accuracy of the dilution-based flow-rate determination, as the conservation of mass for both the simulated flue gas and the tracer gas remains valid. The similar convergence pattern observed at elevated

temperature further verifies the robustness and reliability of the inverted tracer-gas method under thermally elevated operating environments.

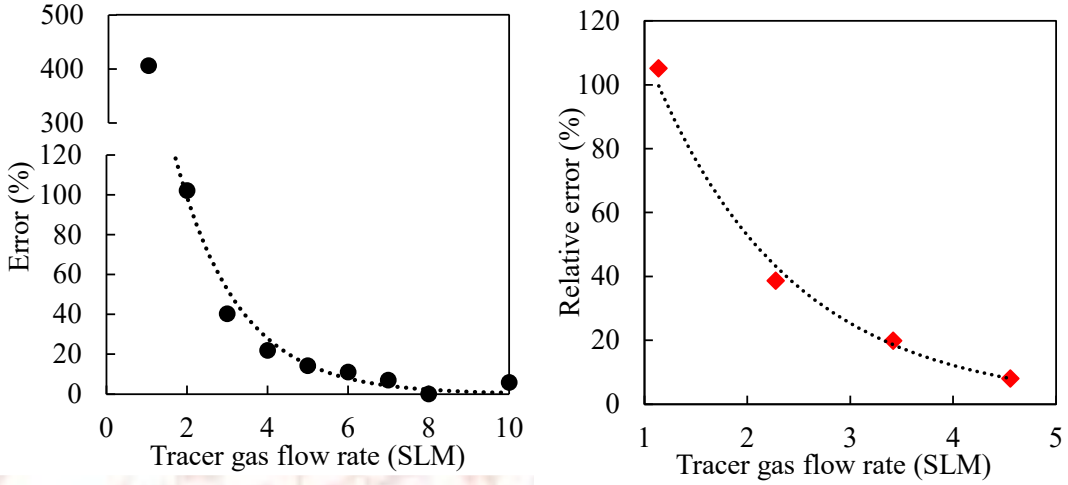

FIGURE 4-3 The errors from the inverted tracer gas method calculation preliminary experiment.

The result shows that the calculated simulated flue gas volume flow rate at room temperature is substantially different from the actual flow rate at a low tracer gas flow rate. A high percentage error (>400%) of the calculated volume flow could be observed at 1 LPM of injecting tracer gas, as shown in FIGURE 4-3 (Left). Then the calculated volume flow rate starts to converge toward the actual original simulated flue gas flow rate (approximately 10 LPM) at the tracer gas flow rate of around 3 SLM. The error decreased significantly to less than 10% at a tracer gas flow rate of 8 SLM onward. The poor accuracy of the flow meter device operating at a low flow rate was thought to cause such an error. Additionally, a low N_2 flow rate developed a low degree of dilution for the whole gas stream, which could result in a certain degree of heterogeneity. These could be the reasons for the inaccuracy at low N_2 injection flow rate. At an elevated temperature of 200 °C, the results showed a similar trend but with an overall improvement in accuracy, as illustrated in FIGURE 4-3 (Right). The relative error decreased exponentially with increasing tracer-gas flow rate, reaching less than 10 % at around 4 SLM. These findings are consistent with the observations reported by Rodney A. Bryant [36] who emphasised that the precision of the tracer-gas dilution technique is highly dependent on the degree of mixing between the injected tracer and the gas stream.

4.3 Real flue gas experiment

This section presents the application of the inverted tracer gas method for calculating the volumetric flow rate under actual flue gas conditions. The flue gas was produced via external combustion using a light oil burner operated at 130% theoretical air. The resulting gas stream was extracted using a custom-built flue gas blower, adapted from the turbine side of an automotive turbocharger. During the experiment, the blower's motor speed was varied between 3500 RPM and 6500 RPM. The flue gas temperature ranged from 383°C to 512°C and exhibited a direct relationship with the flow rate, due to differences in residence time affecting heat loss to the surroundings.

N_2 was employed as the tracer gas and injected downstream of the gas blower at a constant flow rate of 20 LPM.

FIGURE 4-4 (left) displays the CO_2 concentrations of the undiluted flue gas ($C_{CO_{2,0}}$, black dots) and the diluted flue gas ($C_{CO_{2,1}}$, red dots). As the flue gas flow rate increased, the diluted CO_2 concentration ($C_{CO_{2,1}}$) approached that of the undiluted condition ($C_{CO_{2,0}}$). This trend is attributed to the fixed N_2 injection rate, whereby higher flue gas flow rates lead to a reduced degree of dilution. Consequently, the difference between $C_{CO_{2,0}}$ and $C_{CO_{2,1}}$ diminished. The calculated flue gas flow rates, shown in FIGURE 4-4 (right), exhibit a strong linear relationship with motor speed, achieving a coefficient of determination (R^2) of 0.989. This high degree of linearity confirms the reliability and consistency of the proposed inverted tracer gas method under real flue gas conditions.

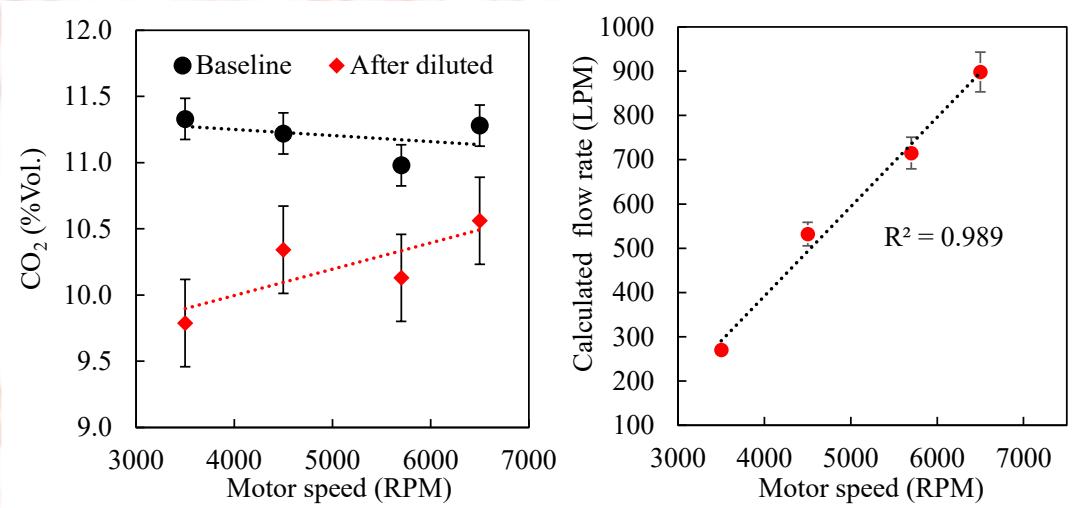

FIGURE 4-4 The measurement of CO_2 concentration in flue gas stream (left), calculated flue gas flow rate (right) as a function of gas blower rotational speed

CHAPTER 5
INTERACTION BETWEEN O_3 AND NO AND THE SUBSEQUENT FORMATION OF NO_2 UNDER VARIABLE PLASMA OPERATING CONDITIONS

In this chapter, the effects of various operating parameters on ozone generation were systematically examined using air as the source gas. The investigation primarily explores how gas flow rate influences ozone yield, as well as how the addition of oxygen (O_2) to air impacts both ozone formation and NO_2 generation. Moreover, the study analyses the influence of applied voltage and frequency on ozone and NO_2 production under air-fed conditions. Subsequently, the ozone produced from air is reacted with NO to study the interactions among NO, NO_2, and O_3. For clarity and coherence, the results and discussion are presented in separate sections according to these experimental focuses.

5.1 Influence of operating parameters (discharge voltage, discharge frequency, O_2 concentration, and gas flow rate) on ozone production.

FIGURE 5-1 and FIGURE 5-2 illustrate the influence of discharge voltage and frequency on O_3 and NO_2 production. The results demonstrated that increased either the discharge voltage or frequency led to a nearly linear rise in both O_3 and NO_2 generation, as shown in FIGURE 5-1(a) and FIGURE 5-1(b). This behaviour corresponds to higher discharge power and a greater rate of energy transfer within the plasma. Elevated the discharge voltage and frequency enhanced the specific energy density (SED) and increased the energy of free charges, thereby promoting oxygen dissociation and subsequent three-body collision reactions [104]. Furthermore, FIGURE 5-1(c) and FIGURE 5-2(C) showed a positive correlation between discharge parameters and both OPE and SOPE, which result from a higher energy density injected into O_2 molecules over time. The O_3/NO_2 ratio (FIGURE 5-1(d)) and (FIGURE 5-2(d)) also increased with voltage and frequency to a certain point, indicating a dominance of ozone formation under enhanced discharge conditions.

To examine the effect of gas flow rate on O_3 and NO_2 production, compressed air flow was varied from 10 to 50 LPM the GHSV and residence time corresponding to TABLE 5-1 Variation of gas residence time with gas hourly space velocity., at a constant voltage of 14 kV_{pp} and 100 Hz. As shown in FIGURE 5-3(a), both O_3 and NO_2 concentrations decreased as the flow rate increased. At the lowest rate of 10 LPM, the ozone and NO_2 concentrations reached 312 ppm and 156.5 ppm, respectively. The decline in concentration with higher flow rates was initially nonlinear but became more proportional at higher rates. This behaviour can be attributed to the reduced residence time of oxygen molecules in the discharge region, which lowers the effective specific energy density and limits the completion of reactions that decompose an atom of oxygen and form ozone, thereby suppressing ozone generation [105].In addition, NO_2 is formed through the oxidation of nitrogen present in air via the $N_2 + O_2 \rightarrow NO_2$ pathway, which consumes part of the discharge energy that would otherwise contribute to ozone formation. Consequently, higher flow rates reduce O_3 concentration, whereas lower flow rates, offering longer residence times, promote ozone formation but also favour increased NO_2 generation. The ozone production rate (OPR), presented in FIGURE 5-3(b), OPR

increased as the flow rate decreased, with a maximum of 0.0062 g/min, while the highest OPE and SOPE values were 17.27 g/J and 0.85 g/J, respectively shown in FIGURE 5-3(c). Finally, the O_3/NO_2 ratio (FIGURE 5-3(d)) decreased with increasing flow rate, indicated that shorter gas residence times limit ozone formation more strongly than NO_2 production.

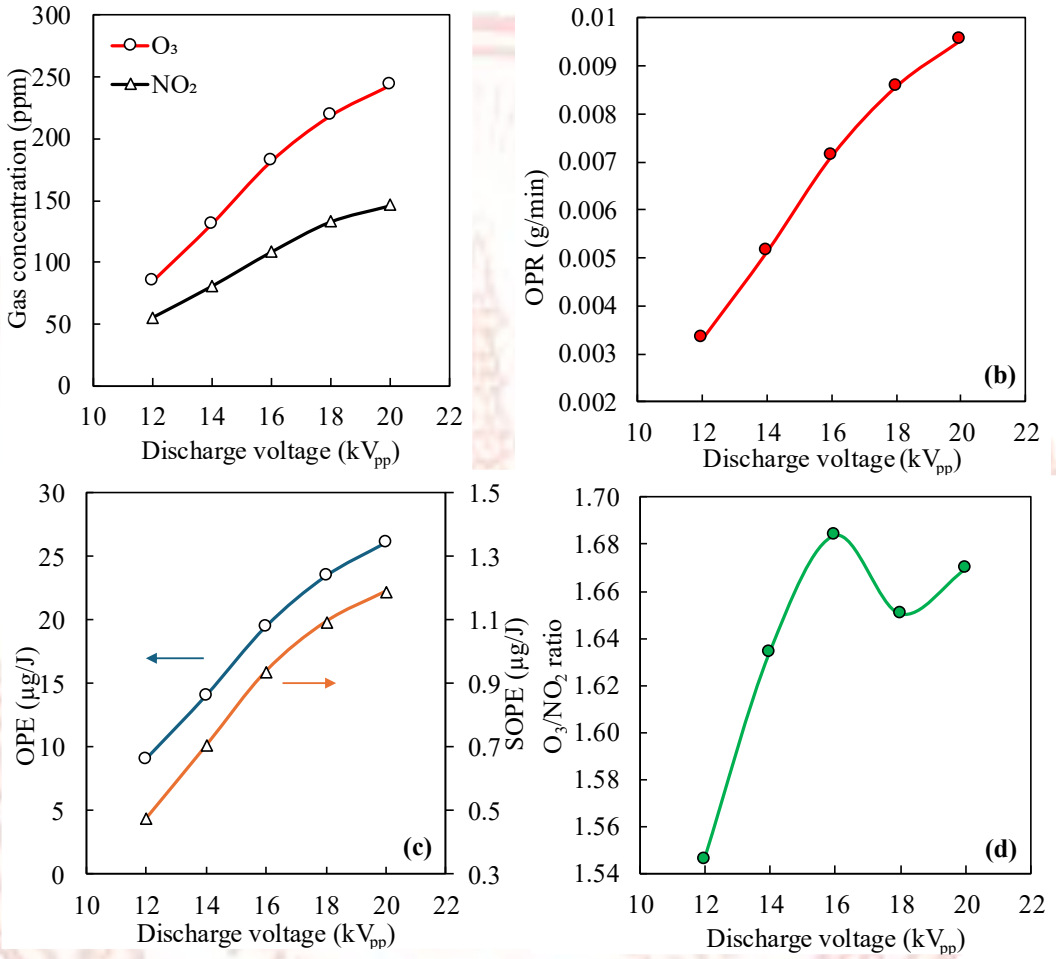

FIGURE 5-1 Effect of discharge voltage of DBD on O_3 and NO_2 using compressed air (20 LPM) at 100 Hz.

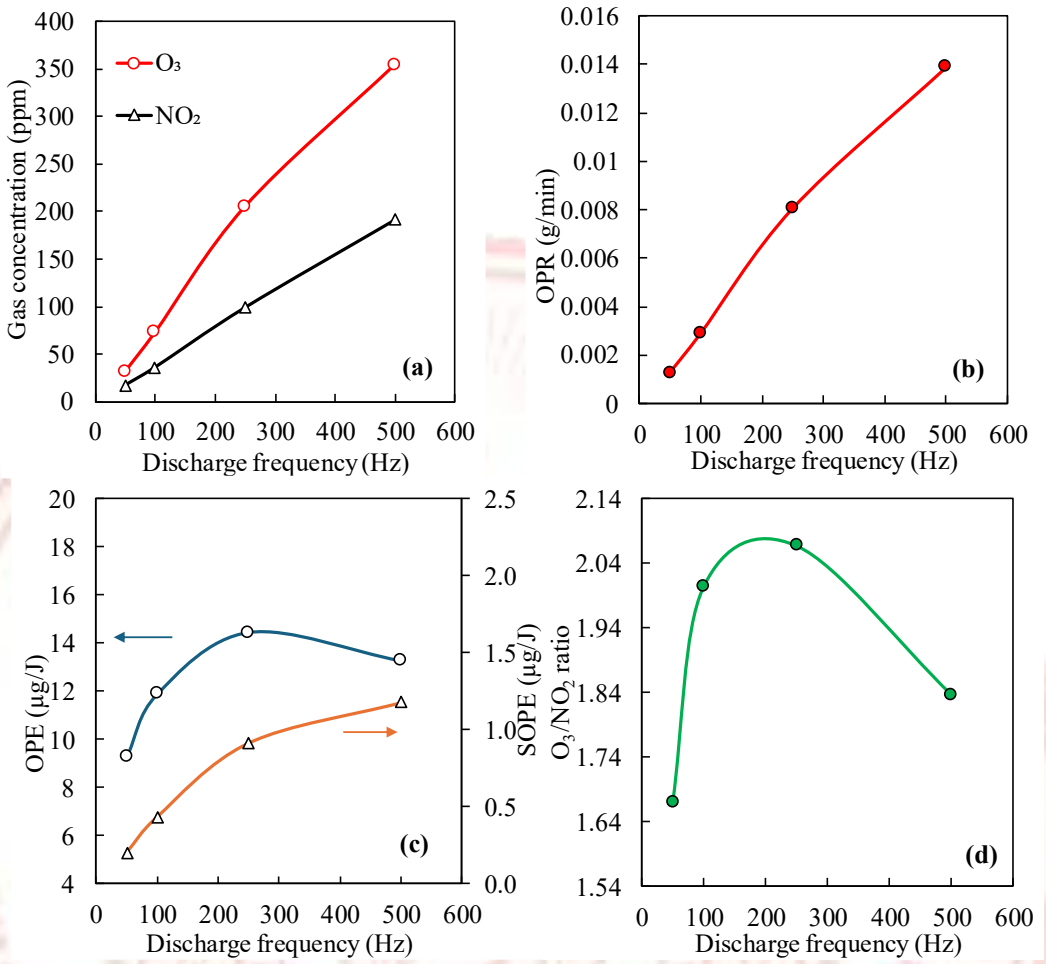

FIGURE 5-2 Effect of discharge frequency of DBD on O_3 and NO_2 using compressed air (20 LPM) at 12 kV_{pp}.

The feed gas employed for examining O_3 and NO_2 production consisted of oxygen–air mixtures, with oxygen concentrations varied between 25 and 65 %-vol. The total flow rate of the mixed gases was maintained at 20 LPM as a controlled parameter. The discharge voltage and frequency were fixed at 12 kV_{pp} and 100 Hz, respectively. As illustrated in FIGURE 5-4(a), both O_3 and NO_2 concentrations increased linearly with the rise in oxygen concentration, reaching a maximum of 184 ppm at 60 %-vol. of O_2, representing an increase of approximately 114 %. This enhancement was attributed to the greater availability of oxygen molecules for collision and reaction. Moreover, oxygen possesses a lower ionisation energy (12 eV) than nitrogen (15 eV) [106], facilitating electron impact dissociation and the formation of reactive oxygen species, which in turn promote ozone generation and subsequent oxidation of NO to NO_2 even at elevated oxygen levels [107]. These observations highlight the crucial role of oxygen concentration in determining ozone formation efficiency. FIGURE 5-4(b) and FIGURE 5-4(c) further demonstrated that increasing the O_2 fraction from 25 %-vol to 60 %-vol markedly enhanced both the OPR and OPE. At 60 % O_2, the SOPE reached 0.863 g/J, while the OPE attained 29.09 µg/J. Finally, FIGURE 5-4(d) presents the O_3/NO_2 ratio, which rose from 1.70 to 1.83 as the oxygen concentration increased from 25 %-vol to 40 %-vol. Beyond this range, the ratio exhibited only a slight further increase,

suggesting that the effect of oxygen enrichment becomes less pronounced at higher concentrations.

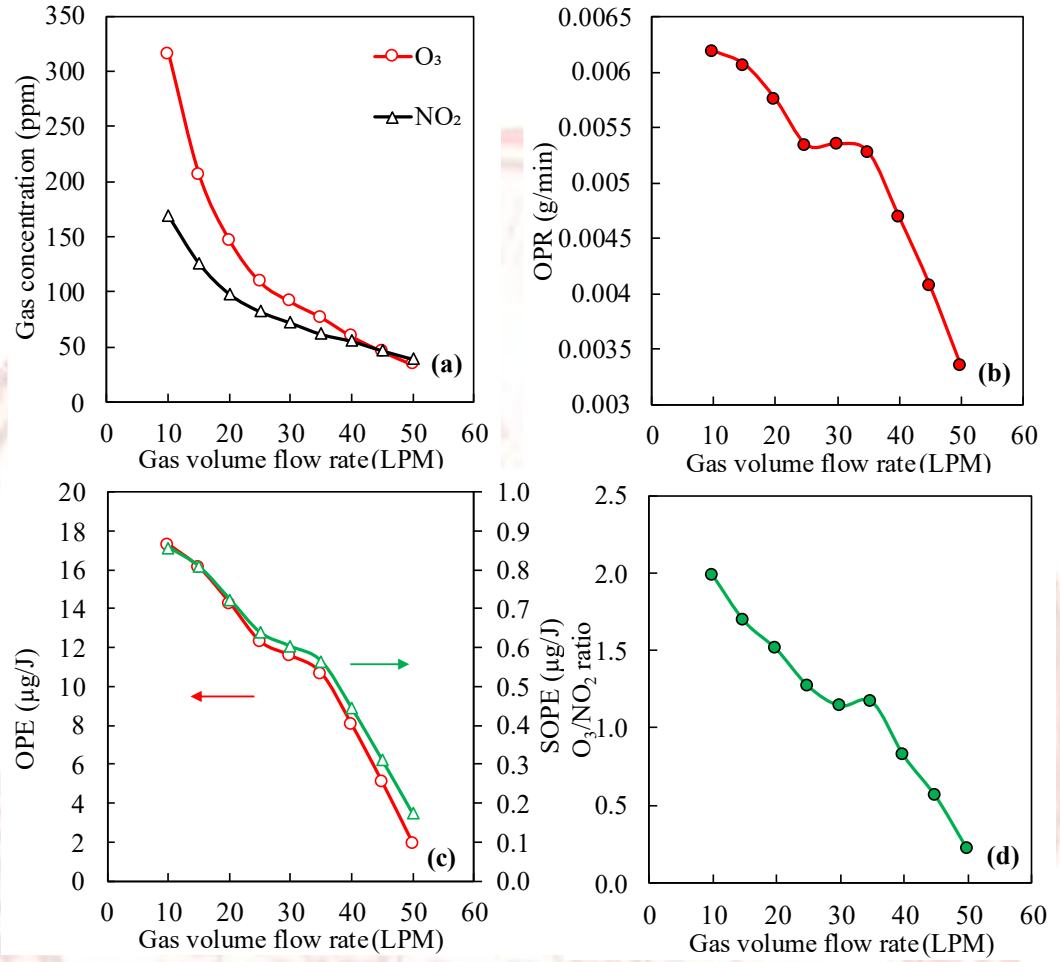

FIGURE 5-3 Effect of gas flow rate of DBD on O_3 production and NO_2 formation at 14 kV_{pp} and 100 Hz.

TABLE 5-1 Variation of gas residence time with gas hourly space velocity.

Gas flow rate (LPM)	GHSV (H^{-1})	Residence time (ms)
10	17427	206.58
15	26140	137.72
20	34853	103.29
25	43567	82.63
30	52280	68.86
35	60993	59.02
40	69707	51.65
45	78420	45.91
50	87133	41.32

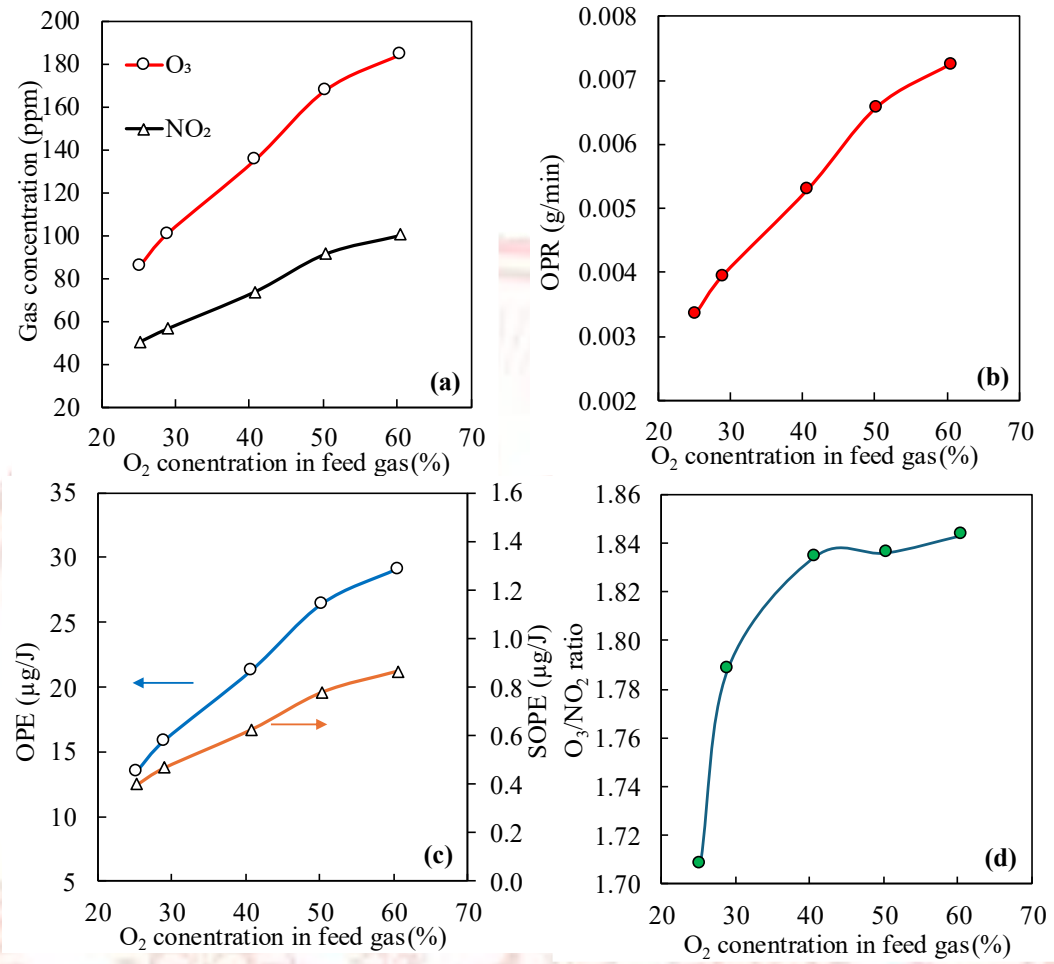

FIGURE 5-4 Effect of oxygen concentration in the feed source gas of DBD reactor on ozone production and NO_2 formation at a discharge voltage of 12 kV_{pp} and frequency of 100 Hz.

5.2 Reaction Pathways of O_3, NO, and NO_2 Formation

The present study examined the influence of input ozone concentration on the oxidation of NO to NO_2. Initially, bottled NO gas was introduced into the reaction chamber along with air while the high-voltage power supply (HVPS) remained switched off to establish the baseline NO concentration. Once the HVPS was activated, non-thermal plasma was active, leading to the production of ozone. The produced O_3 subsequently reacted with NO, facilitating its oxidation to NO_2 while simultaneously consuming part of the ozone. As illustrated in FIGURE 5-5, the NO concentration progressively decreased with increasing input ozone, whereas the NO_2 concentration exhibited a corresponding rise. Complete conversion of NO was achieved when the $O_3/NO \approx 1.66$. However, beyond this level, the NO_2 concentration began to decline, which is likely attributed to further oxidation of NO_2 by ozone to form dinitrogen pentoxide (N_2O_5) through the following reaction pathways R (6-1) and R (6-2) [108]:

$$NO_2 + O_3 \rightarrow NO_3 + O_2 \qquad \text{R (6-1)}$$

$$NO_2 + NO_3 + M \rightarrow N_2O_5 \qquad \text{R (6-2)}$$

These results suggested that while increasing ozone concentration enhances NO oxidation up to the stoichiometric point (O_3/NO ≈ 1.66), excessive ozone input promotes the formation of higher nitrogen oxides, reducing the apparent NO_2 yield.

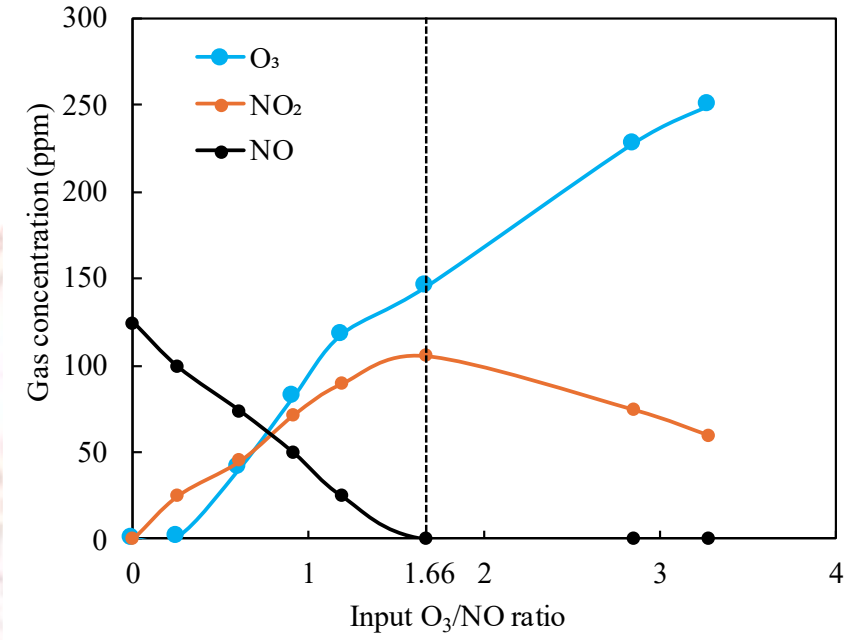

FIGURE 5-5 The reaction of NO oxidation by O_3 and NO_x formation

CHAPTER 6
UPSCALED DBD-NTP OZONE GENERATION

This chapter provides a comprehensive characterisation of the electrical behaviour, energy efficiency, and scaling performance of the multi-cell dielectric barrier discharge (DBD) reactors. The investigation focuses on how discharge dynamics, reactor capacitance. Collectively influence ozone generation behaviour. Through detailed analysis of voltage–charge (Lissajous) characteristics, power consumption, and ozone yield trends, the chapter establishes the interrelationship between plasma discharge conditions and ozone formation efficiency. Furthermore, the scaling effects from single-cell to multi-cell configurations are systematically evaluated to determine how increasing the effective discharge volume and capacitive load affects both ozone production rate and overall energy utilisation.

6.1 Electrical behaviour

FIGURE 6-1 Effect of the capacitor on discharge voltage and current waveform. presents the discharge voltage and current waveforms of the one-, two-, and three-cell DBD configurations operated at 40 kV_{pp} and 100 Hz. Distinct variations in the voltage waveform are evident as the number of DBD cells increases. In the single-cell configuration, the voltage waveform exhibited a slightly distorted square shape, primarily due to the limited slew rate of the high-voltage power supply (HVPS, 800 V μs^{-1}) and the character of the capacitance load. In contrast, the two- and three-cell configurations displayed a markedly gentler voltage slope during both the positive and negative half-cycles. This behaviour arises from the capacitive nature of the DBD reactor, as the overall capacitance increased with the number of dielectric tubes, influencing the reactor's charge–discharge dynamics. For the three-cell arrangement, the maximum attainable voltage was noticeably lower than that of the single- or two-cell setups. This reduction could be attributed to the insufficient charging time within each half-cycle, which limits complete voltage build-up and thereby decreases the effective discharge power. A more detailed analysis of this phenomenon is provided in the following sections. The corresponding current waveforms further revealed that, while the single-cell case produced sharp, narrow pulses, the two- and three-cell configurations generated broader pulses with roughly half the peak amplitude. The maximum discharge current, approximately 60 mA, corresponds to the current-limiting (clipping) threshold of the HVPS. In addition, as the number of cells increased, the current waveform shifted progressively toward a leading-phase characteristic. Overall, the ability of the Trek 20/20C-HS supply to deliver high-voltage signals is constrained by its finite slew rate requiring about 50 μs to reach 40 $kV_{pp,}$ when combined with the increased capacitive loading of the multi-cell reactor, restricts the rapid current delivery necessary for full reactor charging within each cycle.

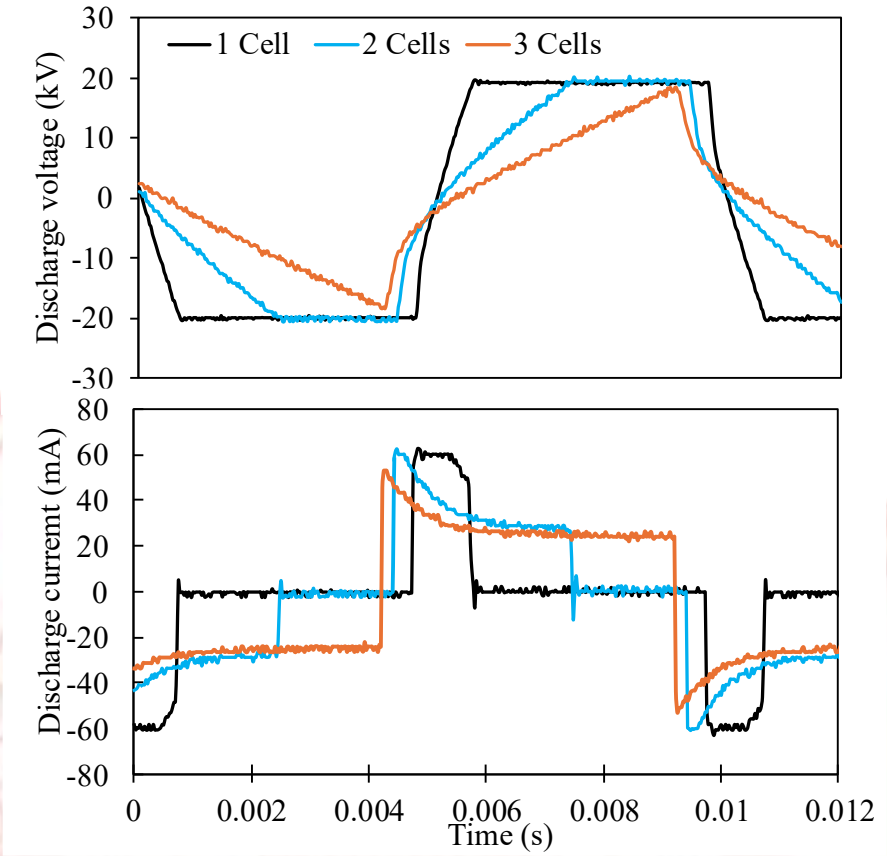

FIGURE 6-1 Effect of the capacitor on discharge voltage and current waveform.

The dielectric characteristics of the DBD reactors were further examined through Lissajous charge–voltage (Q–V) plots, which offer valuable insight into the capacitive behaviour and energy dissipation of the multi-cell system. As illustrated in FIGURE 6-2, the slope of each Q–V curve (dQ/dV) represents the effective dielectric capacitance of the reactor [109]. Linear regression of the plotted data yielded capacitance values of approximately 471.1 pF, 998.39 pF, and 1219.2 pF for the single-, double-, and triple-cell configurations, respectively. These values exhibit a nearly proportional increase with the number of DBD cells, confirming the expected additive nature of capacitance in parallel-connected dielectric assemblies.

Furthermore, the area enclosed by each Lissajous parallelogram corresponds to the energy dissipated per discharge cycle shown in FIGURE 6-2 Lissajous diagram of multi-cell DBD. When operating at a voltage of $40kV_{pp}$ and 100 Hz. As the number of DBD cells increases, this enclosed area expands markedly, indicating greater discharge power and enhanced energy transfer into plasma. This trend reflects the combined effect of increased dielectric surface area and discharge volume, both of which facilitate more frequent micro-discharge events and, consequently, higher ozone generation potential within the multi-cell configuration.

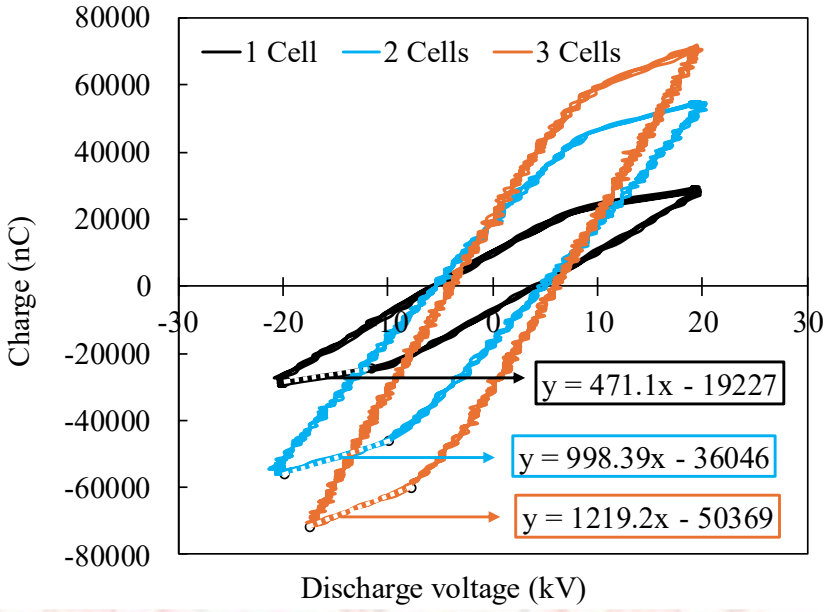

FIGURE 6-2 Lissajous diagram of multi-cell DBD. When operating at a voltage of 40kV$_{pp}$ and 100 Hz.

6.2 Ozone quantification technique and NO_x formation as a byproduct from air feedstock

FIGURE 6-3 presents the FTIR spectra recorded during ozone generation using the three-cell DBD reactor operated at applied voltages of 24, 30, and 40 kV$_{pp}$, under a fixed frequency of 100 Hz with an air + O_2 feed flow of 12 LPM. The spectra clearly displayed the characteristic absorption bands associated with ozone, alongside minor features corresponding to by-product species derived from nitrogen present in the air feed, such as nitrous oxide (N_2O), dinitrogen pentoxide (N_2O_5), and carbon dioxide (CO_2). The absorption regions for these species are summarised in TABLE 6-1 Reference Infrared Absorption Bands of Ozone and Related Species.. At the lowest applied voltage of 24 kV$_{pp}$, the ozone absorption band was relatively weak, suggesting limited plasma energy and low ozone generation efficiency. When the discharge voltage was increased to 30 kV$_{pp}$, a marked enhancement in ozone absorbance was observed, while at 40 kV$_{pp}$, the ozone peak became distinctly dominant over the other spectral features. This progressive increase in ozone signal intensity confirms the strong dependence of ozone formation on discharge strength. The observed trend aligns with the expectation that higher applied voltages elevate the mean electron energy and density within the discharge region, thereby facilitating more effective oxygen dissociation and subsequent three-body recombination processes responsible for ozone formation.

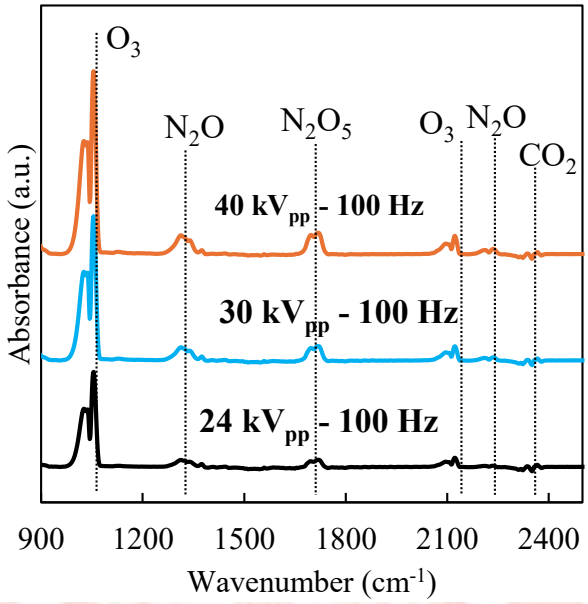

FIGURE 6-3 FTIR spectra of ozone generation at 3 cells configuration.

TABLE 6-1 Reference Infrared Absorption Bands of Ozone and Related Species.

Species	Band (cm^{-1})	Ref
O_3	1050, 2100	[110]
N_2O	1300, 2211, 2237	
N_2O_5	1247, 1720	[76]
CO_2	2360, 2340	

The formation of NO_x species originated from nitrogen present in the air feed, proceeding through several plasma-induced reaction pathways. N_2O is primarily produced via reactions R (7-1) to R (7-2), while N_2O_5 is formed through subsequent reactions R (7-3) to R (7-6) [76]:

$$N_2^* + O_2 \rightarrow N_2O + O \quad \text{R (7-1)}$$

$$NO_2 + N_2 \rightarrow N_2O + O \quad \text{R (7-2)}$$

$$N + O_2 \rightarrow NO + O \quad \text{R (7-3)}$$

$$NO + O_3 \rightarrow NO_2 + O_2 \quad \text{R (7-4)}$$

$$NO_2 + O_3 \rightarrow NO_3 + O_2 \quad \text{R (7-5)}$$

$$NO_2 + NO_3 + M \rightarrow N_2O_5 \quad \text{R (7-6)}$$

The ozone analyser (SKZ1050) used in this investigation had a maximum detection limit of 5000 ppm (vol), making it unsuitable for direct measurement at higher ozone concentrations. To overcome this limitation, the FTIR spectrometer was calibrated against the SKZ1050 to extend the quantifiable range. The calibration was achieved by correlating the analyser readings with the integrated absorbance area of the ozone band obtained from the FTIR spectra. As shown in FIGURE 6-4 Calibration curve for ozone concentration quantity., the resulting calibration curve exhibited an

excellent linear correlation, expressed as y = 615.17x – 63.923, with a coefficient of determination (R^2) of 0.9997. Throughout the experiments, the reactor's discharge power gradually increased, and simultaneous data acquisition from both the ozone analyser and the FTIR system was performed. The strong linearity of the results validates the consistency and precision of the calibration method. This confirms that once the ozone analyser's detection limit is surpassed, FTIR spectroscopy can serve as a reliable and accurate tool for quantifying high ozone concentrations beyond the measurable range of the SKZ1050 analyser.

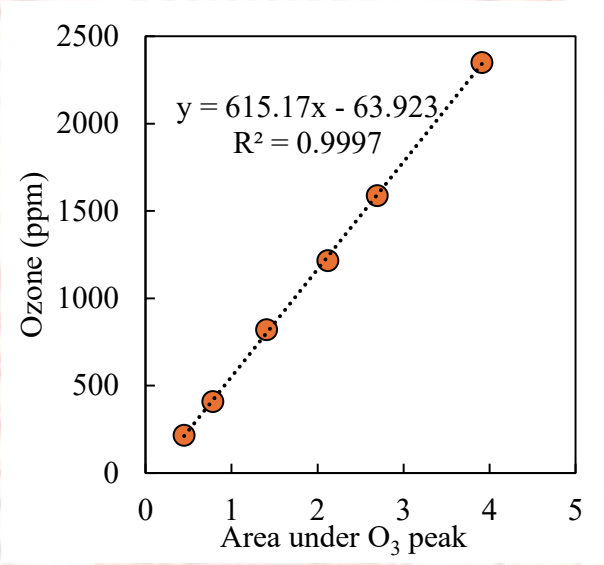

FIGURE 6-4 Calibration curve for ozone concentration quantity.

6.3 Effect of the DBD cells on the ozone production.

FIGURE 6-5 compares the ozone concentrations generated under four different operating conditions (24–40 kV_{pp}, 50–100 Hz) for the one-, two-, and three-cell DBD configurations. The results clearly show that ozone concentration increases with both the number of cells and the applied electrical parameters. Expanding the reactor from one to three cells significantly enhanced ozone generation across all tested voltages and frequencies. This improvement is primarily attributed to the larger effective discharge volume and surface area provided by the additional dielectric tubes, which facilitate a greater number of microdischarge events per cycle. Consequently, a larger proportion of the supplied energy is transferred into plasma-induced reactions, resulting in elevated ozone formation. At an applied voltage of 24 kV_{pp} and a frequency of 50 Hz, the measured ozone concentrations were approximately 1100 ppm, 3100 ppm, and 3500 ppm for the one-, two-, and three-cell reactors, respectively. When the frequency was doubled to 100 Hz under the same voltage, ozone production rose noticeably, reaching about 2200 ppm, 5150 ppm, and 6700 ppm for each configuration in sequence. A similar increasing trend was observed with higher discharge voltages. At both 30 kV_{pp} (50 Hz) and 40 kV_{pp} (100 Hz), ozone concentrations continued to rise across all configurations, confirming that both applied voltage and operating frequency strongly influence ozone generation [111]. The highest concentration was achieved with the three-cell configuration at 40 kV_{pp} and 100 Hz, underscoring the synergistic effect of higher voltage, increased frequency, and reactor scaling on enhancing ozone output.

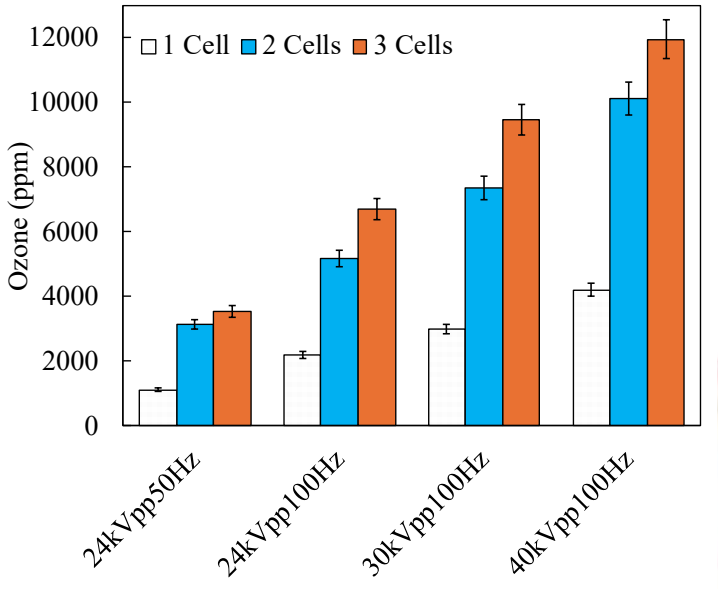

FIGURE 6-5 Compares the ozone production when DBD cells varies for one, two, and three cells in various discharge voltage and frequency.

FIGURE 6-6(a) illustrates the relationship between ozone concentration and specific energy input (SEI) for the one, two, and three-cell DBD reactors. In all configurations, ozone concentration increased linearly with SEI. The three-cell reactor achieved the highest ozone output, reaching 11,946 ppm-vol at 627 J/L, whereas the single-cell configuration produced less than 6000 ppm under the same conditions. However, the concentrations obtained from the two- and three-cell setups were nearly identical within the same SEI range. This convergence is attributed to the limited capability of the high-voltage power supply (HVPS) to deliver sufficient power for fully charging the higher-capacitance three-cell reactor. As shown in FIGURE 6-6(b), the ozone production rate (OPR) exhibited a similar increasing trend with SEI. The three-cell system achieved the highest rate of approximately 0.29 g/min, demonstrating that increasing the number of discharge cells effectively enhances both the discharge volume and ozone yield. In contrast, FIGURE 6-6(c) reveals that the ozone production efficiency (OPE) declined as SEI increased. At lower SEI values (< 100 J/L), the three-cell reactor achieved around 110 µg/J, but as SEI rose to between 340 and 630 J/L, OPE dropped markedly to approximately 38.18 µg/J across all configurations. This reduction in efficiency arises from greater portions of the input energy being dissipated as heat and through other non-productive pathways at higher discharge powers. Although multi-cell systems outperform the single-cell configuration, their relative advantage diminishes under high-energy-input conditions. A distinct trend is observed when evaluating the system ozone production efficiency (SOPE) based on the total system input power, as depicted in FIGURE 6-6(d). Across the studied specific overall energy input (SOEI) range, the two-cell reactor consistently exhibited the highest SOPE (4.46 → 6.21 µg/J), followed by the three-cell (4.06 → 6.27 µg/J) and single-cell (1.84 → 3.84 µg/J) systems. This behaviour highlights the strong dependence of wall-plug efficiency on the HVPS operating characteristics. At low input power, the supply

operated with lower conversion efficiency and poorer power factor. As SOEI increased, the relative electrical losses diminished, improving apparent efficiency. The slightly lower SOPE of the three-cell reactor compared with the two-cell configuration results from its higher capacitive load, which pushed the HVPS beyond its current and slew-rate limits. This condition, evident from broadened current pulses and reduced voltage gradients, caused additional energy losses and prevented full utilisation of the increased discharge capacity. Overall, SOPE provides a more realistic indicator of the system-level energy cost of ozone generation from a practical, end-user perspective, whereas OPE reflects only the intrinsic plasma-based efficiency of the reactor.

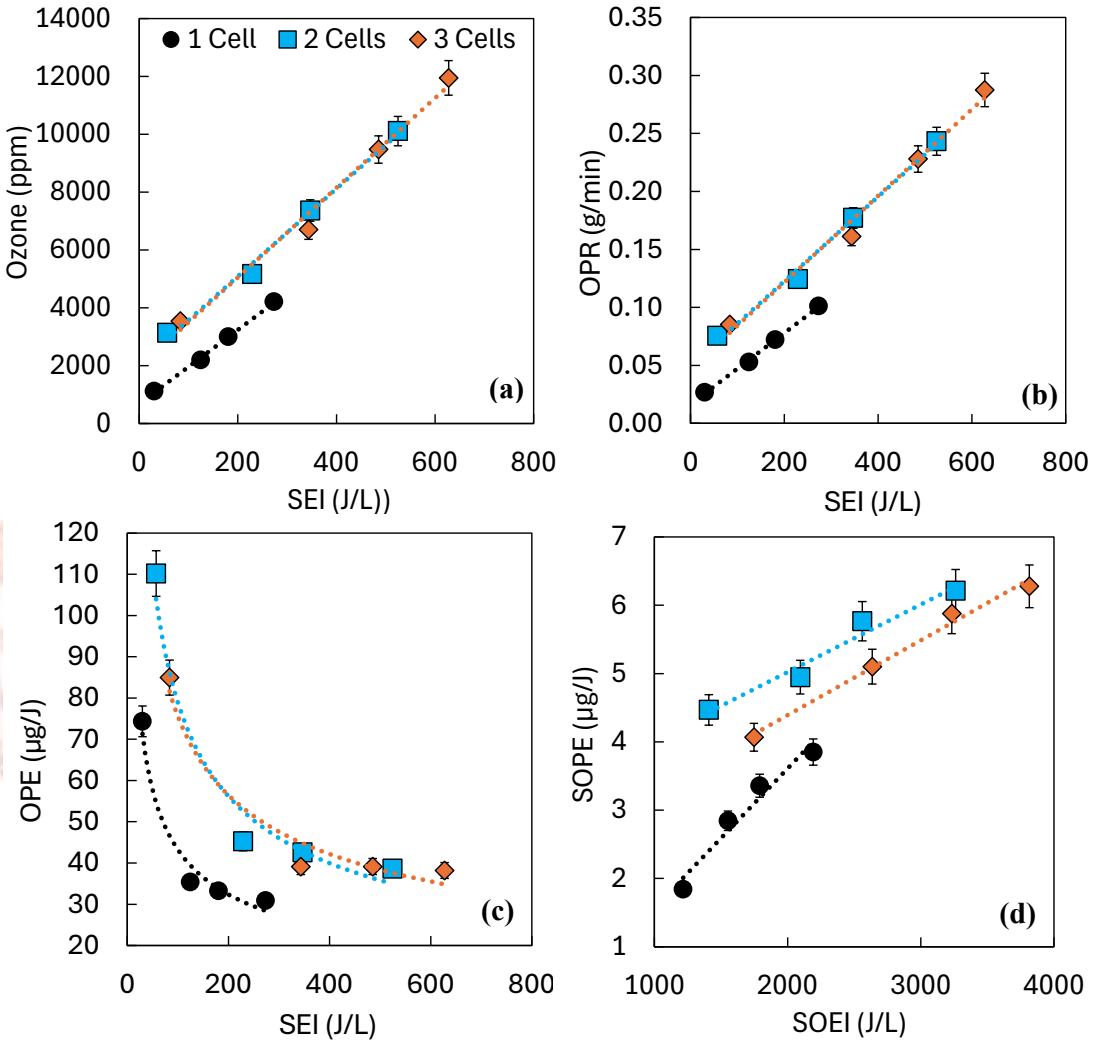

FIGURE 6-6 The Ozone production as a function of specific energy input, expressed in terms of (a) concentration (ppm), (b) ozone production rate (g/min), (c) ozone production efficiency (µg/J) and (d) system ozone production efficiency.

CHAPTER 7
OZONE PROMOTES NO TO NO_2 IN REAL FLUE GAS GENERATED FROM A DIESEL BURNER

The conversion of NO to NO_2 represents a key intermediate step toward efficient NO_x abatement in post-combustion processes. Although the oxidation can proceed thermally or catalytically, the reaction rate and efficiency are limited at high temperatures typical of exhaust gas streams. O_3, a strong oxidant, has been widely recognised as an effective reagent for oxidising NO to NO_2 under NTP environments. This section presents the experimental results on the oxidation of NO contained in real diesel flue gas using ozone generated by a DBD reactor.

7.1 Oxidation of NO to NO_2 in actual flue gas streams through ozone treatment.

After establishing the ozone generation characteristics, the diesel oil burner was ignited and allowed to reach a steady-state condition where both the flue gas temperature and composition remained stable. Ozone, generated by the DBD reactor, was injected into the flue gas stream at rates ranging from 0.015 to 0.08 g/min with the injection point located approximately 80 cm upstream of the sampling port, equivalent to about 13 times the inner diameter of the flue gas pipe. This configuration ensured allowable mixing and reaction between ozone and NO. As the ozone injection rate increased, the NO concentration decreased, indicating effective oxidation of NO to NO_2 depicted in FIGURE 7-1(a). From the linear correlation obtained, complete oxidation of NO required an ozone feed rate of approximately 0.08 g/min, corresponding to an O_3/NO ratio of 6.15 as shown in FIGURE 7-1(b). According to the relation $NO+O_3 \rightarrow NO_2+O_2$. At O_3/NO ratio of 1.0 would theoretically be required. However, under actual flue gas conditions, nearly fivefold excess ozone was necessary to achieve complete oxidation. This discrepancy was attributed to the high temperature of the flue gas, which accelerated ozone decomposition through $O+O_2 \leftrightarrow O_3$ and $O_3 +O \rightarrow 2O_2$, as well as the short residence time (≈ 831 ms) available for the O_3 and NO reaction in the flow path. When the O_3/NO ratio exceeded the stoichiometric requirement, NO_2 was further oxidised to higher oxides such as NO_3, eventually forming N_2O_5 via $NO_2 +NO_3 \rightarrow N_2O_5$. For selective catalytic reduction (SCR) enhancement, complete NO oxidation is unnecessary. Converting about 50 % of NO to NO_2 (NO_2/NO ≈ 1) provides the optimal balance for the fast-SCR reaction. As shown in FIGURE 7-1(C), this occurs at an ozone injection rate of 0.027 g/min, corresponding to an O_3/NO ratio of 2.35 and a NO conversion efficiency of 0.304 μg/J. This moderate ratio effectively reduces excess ozone consumption while improving overall energy efficiency.

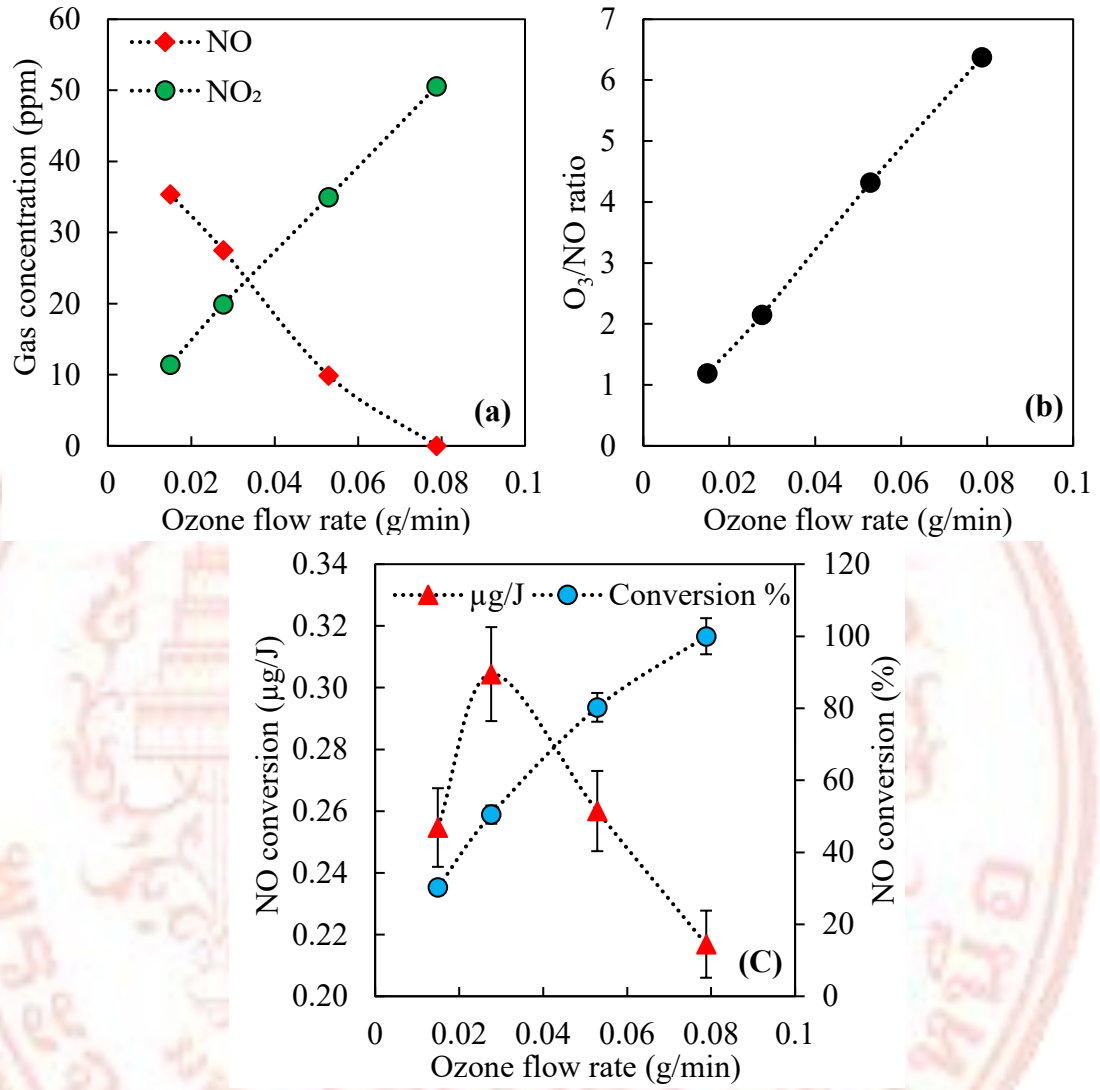

FIGURE 7-1 Effect of ozone injected into flue gas on promoting NO to NO_2 at a flue gas flow rate of 270 LPM.

FIGURE 7-2 illustrates the influence of flue gas flow rate on NO_x behaviour when a constant ozone injection rate of 0.055 g/min was supplied. Increasing the flue gas flow introduced a larger quantity of NO within a given time FIGURE 7-2(a), thereby reducing the O_3/NO ratio FIGURE 7-2(b). As a result, a portion of NO remained unoxidised because the fixed ozone supply could only convert a limited fraction of the available NO, as reflected by the corresponding NO_2 concentrations in FIGURE 7-2(a). At higher flow rates, the flue gas temperature rose owing to the shorter residence time of hot gas in contact with the pipe wall, which reduced heat dissipation. FIGURE 7-2(c) demonstrates an inverse relationship between flue gas temperature and residence time within the reaction zone. The combined effects of increased gas temperature and reduced O_3/NO ratio led to greater ozone decomposition [112], less effective NO oxidation, and decreased NO_2 formation. Under these conditions, a flow rate of 750 LPM achieved approximately 50 % NO conversion with a peak conversion efficiency

of 0.815 µg/J. Further increases in flow rate caused a decline in both NO conversion percentage and energy efficiency FIGURE 7-2(d).

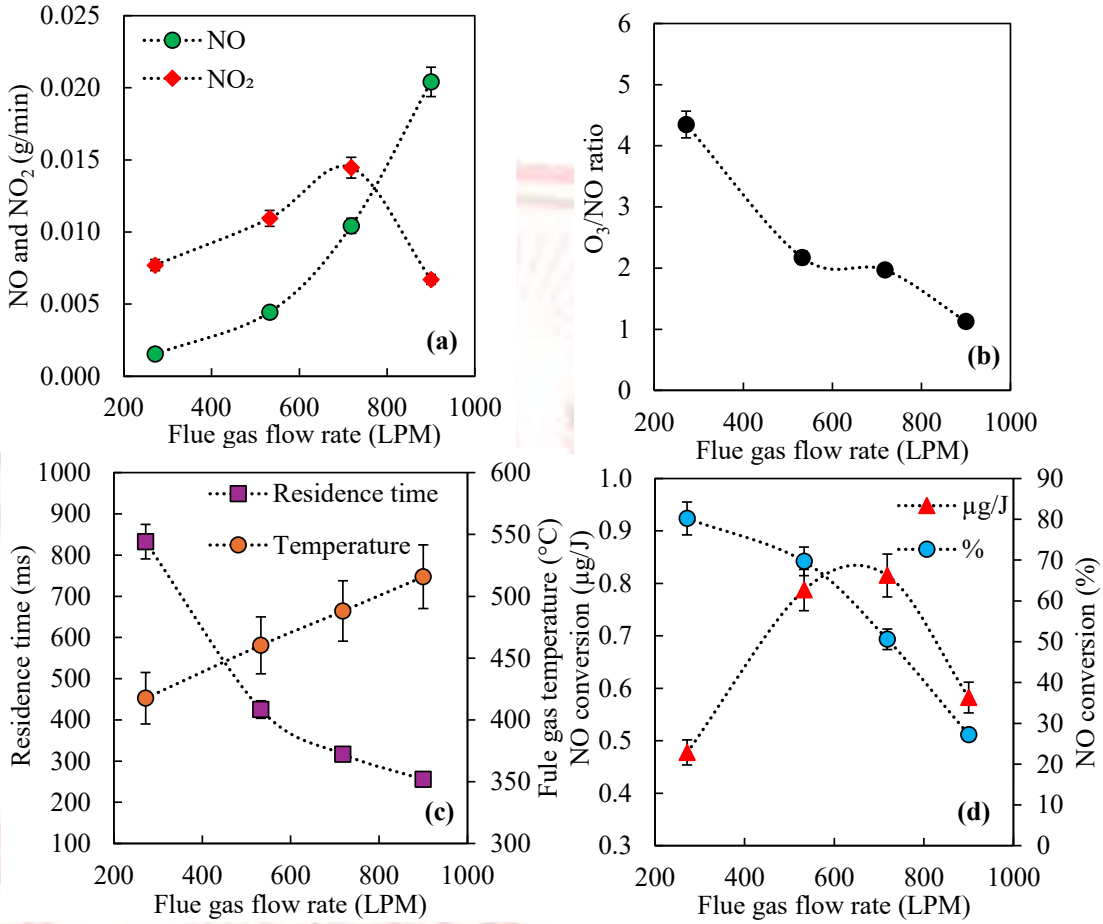

FIGURE 7-2 Effect of flue gas flow rate on promoting NO to NO_2.

CHAPTER 8
CONCLUSION AND FUTURE WORK

8.1 Conclusion

This research demonstrated the use of a (DBD-NTP) system for NO_x abatement in flue gas applications, combining both ozone generation and its subsequent application for NO oxidation with ozone. A systematic experimental investigation was carried out, encompassing verification of the inverted tracer-gas method for accurate volumetric flow measurement of flue gas, and investigation of ozone generation characteristics under various operating parameters of DBD-NTP. furthermore, investigation of up-scaling of DBD reactors, and finally, the application of ozone for the oxidation NO in real flue-gas conditions.

The inverted tracer-gas technique was verified as a reliable and economical method for determining volumetric flow rates of simulated and real flue gases. Strong linear correlations between the tracer-gas flow rate and CO_2 dilution ($R^2 \approx 0.99$) were maintained across ambient and elevated temperatures up to 210 °C, confirming thermal robustness. The method's accuracy improved significantly at higher tracer-gas injection rates (> 4 SLM), where percentage error fell below 10 %. This validated procedure was subsequently employed to measure diesel-flue-gas flow, ensuring precise calculation of specific energy input and NO_x conversion efficiency in later plasma–oxidation experiments.

Ozone generation experiments using the DBD-NTP reactor revealed that discharge voltage, frequency, oxygen fraction in the feed gas, and gas-flow rate significantly influenced both the ozone production yield and the ozone production efficiency. Higher voltages and frequencies enhanced ozone formation as a result of intensified microdischarge activity, higher electron-impact energy, and increased rates of oxygen dissociation and three-body recombination reactions. Conversely, excessive gas-flow rates reduced residence time in the discharge region, leading to a lower degree of ozone formation. The ozone can completely oxidise NO at an O_3/NO ratio of 1.66, at a higher O_3/NO ratio, the NO can lead to NO_3 and N_2O_5 subsequently. The DBD-NTP reactor scaling investigation demonstrated that increasing the number of DBD cells significantly enhanced ozone generation performance. Ozone concentration increased linearly with specific energy input, reaching ≈ 11946 ppm at 627 J/L for the three-cell configuration, while the ozone-production rate (OPR) attained ≈ 0.29 g/min. However, the ozone-production efficiency (OPE) declined with rising energy input from ≈ 110 µg/J (below 100 J/L) to ≈ 38 µg/J at higher discharge powers due to energy losses as heat. The system ozone-production efficiency (SOPE) based on wall-plug power indicated the best performance for the two-cell reactor, yielding 4.46 – 6.21 µg/J, compared with 4.06 – 6.27 µg/J for the three-cell and 1.84 – 3.84 µg/J for the single-cell. The three-cell reactor's higher capacitance (≈ 1219 pF) imposed load on the Trek 20/20C-HS power supply, restricting voltage slew rate and causing waveform distortion. Overall, up-scaling DBD reactors improves ozone yield, but optimum efficiency is achieved with the two-cell configuration, balancing discharge volume and power-supply capability.

Subsequent experiments demonstrated that ozone effectively oxidised NO to NO_2 in real diesel-flue-gas environments. Increasing the ozone feed from 0.015 to 0.08

g/min reduced NO and raised NO_2 concentrations, reaching complete conversion NO at an O_3/NO ratio of ≈ 6.15. The higher-than-stoichiometric requirement resulted from ozone decomposition at elevated gas temperatures (≈ 480–520 °C) and the short residence time (~ 0.83 s). Optimum ozone performance occurred at 0.027 g/min (O_3/NO ≈ 2.35), achieving 50 % NO-to-NO_2 conversion with 0.304 µg/J, favourable for the fast-SCR pathway. At a fixed ozone rate of 0.055 g/min, increasing the flue-gas flow (270–900 LPM) lowered the O_3/NO ratio and residence time, accelerating ozone decomposition and reducing conversion efficiency. The best overall performance was obtained at ≈ 750 LPM, giving ≈ 50 % conversion and 0.815 µg/J efficiency. These findings verified that plasma-generated ozone can serve as an efficient pre-oxidant, facilitating fast-SCR reactions downstream and enabling lower-temperature operation of catalytic systems.

Overall, this study demonstrates that DBD-NTP technology offers a promising, low-temperature, and effective method for NO_x mitigation. Its modular design, scalability, and compatibility with existing exhaust-treatment systems make it highly suitable for integration into power-generation and industrial emission-control processes. Furthermore, the detailed analysis of the electrical–chemical interactions presented in this study provides a valuable framework for optimising plasma-based pollutant-control systems. When integrated with other after-treatment technologies, such as SCR, the plasma-generated oxidants can enhance the overall efficiency and $DeNO_x$ yield.

8.2 Future work

Future research should focus on advancing the performance, scalability, and integration potential of DBD-NTP systems for practical flue-gas treatment. Further optimisation of the electrical circuit and reactor geometry is necessary to improve power coupling efficiency under high-capacitance loads and to maintain discharge stability during up-scale operation. Integration of the DBD-NTP with catalytic after-treatment systems such as SCR or oxidation catalysts could enhance overall NO_x conversion efficiency and selectivity toward N_2 formation.

REFERENCES

1. Agency, E. E. (2023). [Online]. Emissions and energy use in large combustion plants in Europe. [Retrieved Day Month 2023]. From https://www.eea.europa.eu/en/analysis/indicators/emissions-and-energy-use-in?activeAccordion=546a7c35-9188-4d23-94ee-005d97c26f2b
2. Mofijur, M., et al. (2012). "Prospects of biodiesel from Jatropha in Malaysia." Renewable and Sustainable Energy Reviews. 16 7: 5007-5020.
3. Agency, E. P. (2021). [Online]. Overview of Greenhouse Gases. [Retrieved Day Month 2021]. From https://www.epa.gov/ghgemissions/overview-greenhouse-gases
4. Wang, M., et al. (2025). "Particulate matter air pollution as a cause of lung cancer: epidemiological and experimental evidence." Br J Cancer. 132 11: 986-996.
5. Puett, R. C., et al. (2014). "Particulate matter air pollution exposure, distance to road, and incident lung cancer in the nurses' health study cohort." Environ Health Perspect. 122 9: 926-932.
6. West, J. J., et al. (2016). ""What We Breathe Impacts Our Health: Improving Understanding of the Link between Air Pollution and Health"." Environ Sci Technol. 50 10: 4895-4904.
7. Xiao, G., et al. (2014). "Non-Thermal Plasmas for VOCs Abatement." Plasma Chemistry and Plasma Processing. 34 5: 1033-1065.
8. Shan, W., et al. (2021). "Theory and practice of metal oxide catalyst design for the selective catalytic reduction of NO with NH_3
." Catalysis Today. 376: 292-301.
9. Carrasco-Venegas, L. A., et al. (2025). "Mathematical Modeling of Photochemical and Chemical Interactions in Photochemical Smog Formation." Processes. 13 5.
10. Fathima, N.). "EFFECTS OF PHOTOCHEMICAL SMOG AND MANAGEMENT STRATEGIES." ENGINEERING ENVIRONMENTAL CHEMISTRY. 71.
11. Gholami, F., et al. (2020). "Technologies for the nitrogen oxides reduction from flue gas: A review." Sci Total Environ. 714: 136712.
12. Abdelaal, M., et al. (2021). "Characteristics and flame appearance of oxy-fuel combustion using flue gas recirculation." Fuel. 297.
13. Anufriev, I. S., et al. (2021). "NO_x reduction by steam injection method during liquid fuel and waste burning." Process Safety and Environmental Protection. 152: 240-248.
14. Chen, R., et al. (2021). "Recent advances in simultaneous removal of SO_2 and NO_x from exhaust gases: Removal process, mechanism and kinetics." Chemical Engineering Journal. 420.
15. Goemans, M., et al. (2004). "Catalytic NO_x reduction with simultaneous dioxin and furan oxidation." Chemosphere. 54 9: 1357-1365.
16. Okubo, M. (2021). "Recent Development of Technology in Scale-up of Plasma Reactors for Environmental and Energy Applications." Plasma Chemistry and Plasma Processing. 42 1: 3-33.
17. Muzio, L., Quartucy, G., & Cichanowiczy, J. (2002). "Overview and status of post-combustion NO_x control: SNCR, SCR and hybrid technologies." International Journal of Environment and Pollution. 17 1-2: 4-30.

18. Liu, J., et al. (2019). "Structure, synthesis, and catalytic properties of nanosize cerium-zirconium-based solid solutions in environmental catalysis." Chinese Journal of Catalysis. 40 10: 1438-1487.
19. Li, W.-J., Li, T.-Y., & Wey, M.-Y. (2021). "Preferred enhancement of fast-SCR by Mn/CeSiOx catalyst: Study on Ce/Si promotion and shape dependence." Chemical Engineering Journal. 403.
20. Hyun-Ha, K., et al. (2023). "Revisiting why DBDs can generate O_3 against the thermodynamic limit." International Journal of Plasma Environmental Science & Technology (IJPEST). 17 2: 1-20.
21. Keidar, M. (2013). Plasma Engineering : Applications from Aerospace to Bio and Nanotechnology. Academic Press.
22. Wongchang, T., et al. (2021). "Impact of High-Voltage Discharge After-Treatment Technology on Diesel Engine Particulate Matter Composition and Gaseous Emissions." ACS Omega. 6 32: 21181-21192.
23. Hamed, M. S., Majdi, H. S., & Hasan, B. O. (2020). "Effect of Electrode Material and Hydrodynamics on the Produced Current in Double Chamber Microbial Fuel Cells." ACS Omega. 5 18: 10339-10348.
24. Adelodun, A. A. (2020). "Influence of Operation Conditions on the Performance of Non-thermal Plasma Technology for VOC Pollution Control." Journal of Industrial and Engineering Chemistry. 92: 41-55.
25. Yao, S. (2009). "Plasma Reactors for Diesel Particulate Matter Removal." Recent Patents on Chemical Engineering. 2 1: 67-75.
26. Cheong, K. W. (2001). "Airflow measurements for balancing of air distribution system — tracer-gas technique as an alternative?" Building and Environment. 36 8: 955-964.
27. Benjamin, S. F., & Roberts, C. A. (2002). "Measuring flow velocity at elevated temperature with a hot wire anemometer calibrated in cold flow." International Journal of Heat and Mass Transfer. 45 4: 703-706.
28. Liu, Q., et al. (2021). "Development of Flue Gas Audio-Range Velocimeter Using Quadratic-Convex Frequency Sweeping." IEEE Sensors Journal. 21 8: 9777-9787.
29. Weise, J., Baliño, J. L., & Paladino, E. E. (2021). "CFD study of the transient wet gas flow behavior through orifice plate flow meters." Flow Measurement and Instrumentation. 82.
30. Zhang, H., Guo, C., & Lin, J. (2019). "Effects of Velocity Profiles on Measuring Accuracy of Transit-Time Ultrasonic Flowmeter." Applied Sciences. 9 8.
31. Bryant, R. A. (2018). "Uncertainty estimates of tracer gas dilution flow measurements in large-scale exhaust ducts." Flow Meas Instrum. 61.
32. [Record #195 is using a reference type undefined in this output style.]
33. Boadi, D., Wittenberg, K., & Kennedy, A. (2002). "Validation of the sulphur hexafluoride (SF_6) tracer gas technique for measurement of methane and carbon dioxide production by cattle." Canadian Journal of Animal Science. 82 2: 125-131.
34. Han, H. (2012). "Ventilation effectiveness measurements using tracer gas technique." Fluid Dynamics, Computational Modeling and Applications. 41-66.
35. Cheong, K.-W. (1994). "A measurement technique guide on the application of tracer gas techniques for measuring airflow in HVAC systems."

36. Bryant, R. A. (2024). “Exhaust flow calibration for a large-scale calorimetry system using tracer gas dilution.” Fire Mater. 48 2.
37. Cox, L. (1999). Nitrogen oxides (NO_x) why and how they are controlled. Diane Publishing.
38. Merryman, E. L., & Levy, A. (1975). “Nitrogen oxide formation in flames: The roles of NO_2 and fuel nitrogen.” Symposium (International) on Combustion. 15 1: 1073-1083.
39. Wang, Z., & Yang, X. (2024). “NO_x Formation Mechanism and Emission Prediction in Turbulent Combustion: A Review.” Applied Sciences. 14 14.
40. Zeldovich, Y. B. (1992). Princeton: Princeton University Press.
41. Anetor, L., Odetunde, C., & Osakue, E. E. (2014). “Computational Analysis of the Extended Zeldovich Mechanism.” Arabian Journal for Science and Engineering. 39 11: 8287-8305.
42. Maroa, S., & Inambao, F. (2020). The NO_x Formation Routes. Translated by. Cham: Springer International Publishing.
43. Xu, J., Wang, D., & Meng, H. (2023). “Quantitative analyses of NO formations from different reaction pathways in methane-air combustion at various pressures and temperatures.” Fuel. 337.
44. Fenimore, C. P. (1971). “Formation of nitric oxide in premixed hydrocarbon flames.” Symposium (International) on Combustion. 13 1: 373-380.
45. Campos, J., et al. (2024). “NO Formation in Combustion Engines Fuelled by Mixtures of Hydrogen and Methane.” Sustainability. 16 13.
46. Stagni, A., et al. (2022). Chemistry of nitrogen oxides (NO_x) formation in flameless combustion. Translated by.
47. Bozzelli, J. W., & Dean, A. M. (1995). “O + NNH: A possible new route for formation in flames.” International Journal of Chemical Kinetics. 27 11: 1097-1109.
48. Alagumalai, A., et al. (2022). NO_x formation chemical kinetics in IC engines. Translated by.
49. Belch, J., et al. (2021). “Associations between ambient air pollutants and hospital admissions: more needs to be done.” Environmental Science and Pollution Research. 28.
50. Pfeffer, P. E., et al. (2019). “Increased Chronic Obstructive Pulmonary Disease Exacerbations of Likely Viral Etiology Follow Elevated Ambient Nitrogen Oxides.” Am J Respir Crit Care Med. 199 5: 581-591.
51. Carbone, U., et al. (2014). “Respiratory function in power plant workers exposed to nitrogen dioxide.” Occupational Medicine. 64 8: 644-646.
52. Garcia-Gonzalez, H., et al. (2024). “Assessment of NO_x Levels in an Underground Hospital Car Park: Implications for Occupational and Environmental Health.” Applied Sciences. 14 5.
53. Zhang, J. J., Wei, Y., & Fang, Z. (2019). “Ozone Pollution: A Major Health Hazard Worldwide.” Front Immunol. 10: 2518.
54. Nguyen, D.-H., et al. (2022). “Tropospheric ozone and NO_x: A review of worldwide variation and meteorological influences.” Environmental Technology & Innovation. 28.

55. Protection, T. N. J. D. o. E. (2021). [Online]. NO_x and VOC Emission Trends: Ozone Precursors. [Retrieved Day Month 2021]. From https://dep.nj.gov/wp-content/uploads/dsr/trends-nox-voc.pdf
56. Akimoto, H., & Tanimoto, H. (2022). "Rethinking of the adverse effects of NO_x-control on the reduction of methane and tropospheric ozone – Challenges toward a denitrified society." Atmospheric Environment. 277: 119033.
57. Kiendler-Scharr, A., et al. (2016). "Ubiquity of organic nitrates from nighttime chemistry in the European submicron aerosol." Geophysical Research Letters. 43 14: 7735-7744.
58. Shaw, S., & Van Heyst, B. (2022). "An Evaluation of Risk Ratios on Physical and Mental Health Correlations due to Increases in Ambient Nitrogen Oxide (NO_x) Concentrations." Atmosphere. 13 6.
59. Ministry of Natural, R., & Environment. (2023). "Notification of the Ministry of Natural Resources and Environment on Emission Standards for Power Plants B.E. 2566 (2023)." 36-42.
60. Wynn, G., & Coghe, P. (2017). Europe's Coal-Fired Power Plants: Rough Times Ahead.). Cleveland, Ohio, USA.
61. European, C. (2015). Commission welcomes Member States' agreement on robust testing of air pollution emissions by cars. (Press release). Brussels.
62. European, U. (2007). Regulation (EC) No 715/2007 of the European Parliament and of the Council of 20 June 2007 on type approval of motor vehicles with respect to emissions from light passenger and commercial vehicles (Euro 5 and Euro 6) and on access to vehicle repair and maintenance information. (Official Journal of the European Union). Brussels.
63. European, U. (2024). Regulation (EU) 2024/1257 of the European Parliament and of the Council of 24 April 2024 on type-approval of motor vehicles and engines with respect to their emissions and battery durability (Euro 7) and repealing Regulations (EC) No 715/2007 and (EC) No 595/2009. (Official Journal of the European Union). Brussels.
64. Elkaee, S., Phule, A. D., & Yang, J. H. (2024). "Advancements in (SCR) technologies for NOx reduction: A comprehensive review of reducing agents." Process Safety and Environmental Protection. 184: 854-880.
65. Elkaee, S., et al. (2023). "Catalysts for fast and NO_2 SCR reactions for the removal of nitrogen oxides emitted from various sources: Recent advances, mechanisms, and future directions." Journal of Environmental Chemical Engineering. 11 6.
66. González Hernández, N. N., et al. (2020). "Improved NOx Reduction Using and H2 with Ag/Al2O_3 Catalysts Promoted with Pt and WOx." Catalysts. 10 10.
67. Ye, B., et al. (2022). "Recent trends in vanadium-based SCR catalysts for NOx reduction in industrial applications: stationary sources." Nano Converg. 9 1: 51.
68. Szymaszek, A., Samojeden, B., & Motak, M. (2020). "The Deactivation of Industrial SCR Catalysts—A Short Review." Energies. 13 15.
69. Zyrkowski, M., et al. (2020). "Deactivation of −WO_3/TiO_2 $DeNO_x$ Catalyst under Commercial Conditions in Power Production Plant." Energies. 13 23.
70. Geng, J., et al. (2022). "Research progress in the sulfur resistance of catalytic combustion catalysts." Journal of Fuel Chemistry and Technology. 50 5: 564-576.

71. Zhang, Q., et al. (2020). "Influence of preparation methods on iron-tungsten composite catalyst for NH_3-SCR of NO: The active sites and reaction mechanism." Applied Surface Science. 503: 144190.
72. Gao, P., et al. (2021). "Copper in $LaMnO_3$ to promote peroxymonosulfate activation by regulating the reactive oxygen species in sulfamethoxazole degradation." Journal of Hazardous Materials. 411: 125163.
73. Shi, Z., et al. (2023). "Mechanism, performance and modification methods for NH3-SCR catalysts: A review." Fuel. 331.
74. Zhao, S., et al. (2022). "Research progress on selective catalytic reduction (SCR) catalysts for NO removal from coal-fired flue gas." Fuel Processing Technology. 236.
75. Talebizadeh, P., et al. (2014). "The role of non-thermal plasma technique in NO_x treatment: A review." Renewable and Sustainable Energy Reviews. 40: 886-901.
76. Yuan, D., et al. (2016). "Ozone production in parallel multichannel dielectric barrier discharge from oxygen and air: the influence of gas pressure." Journal of Physics D: Applied Physics. 49 45.
77. Nehra, V., & Kumar, A. (2008). "Atmospheric non-thermal plasma sources."
78. Molchanov, O., et al. (2025). "Transformation of NO in Combustion Gases by DC Corona." Fire. 8 1.
79. Zhu, Y., et al. (2020). "A novel simulation method for predicting ozone generation in corona discharge region." Chemical Engineering Science. 227.
80. Molchanov, O., et al. (2024). "Application End Evaluation of Electrostatic Precipitation for Control PM and NO_x Emissions from Small-Scale Combustions." Fire. 7 10.
81. Lebedev, Y. A. (2010). "Microwave discharges: generation and diagnostics." Journal of Physics: Conference Series. 257.
82. Saifutdinov, A. I., & Kustova, E. V. (2021). "Dynamics of plasma formation and gas heating in a focused-microwave discharge in nitrogen." Journal of Applied Physics. 129 2.
83. Chen, G., et al. (2017). "An overview of in a microwave discharge: the role of plasma-catalysis." Journal of Physics D: Applied Physics. 50 8.
84. Kalra, C. S., Gutsol, A. F., & Fridman, A. A. (2005). "Gliding arc discharges as a source of intermediate plasma for methane partial oxidation." IEEE Transactions on Plasma Science. 33 1: 32-41.
85. Baowei, W., et al. (2020). "Gliding arc plasma reforming of toluene for on-board hydrogen production." International Journal of Hydrogen Energy. 45 11: 6138-6147.
86. Jardali, F., et al. (2021). "NO_x production in a rotating gliding arc plasma: potential avenue for sustainable nitrogen fixation." Green Chemistry. 23 4: 1748-1757.
87. Rabinovich, A., et al. (2021). "Scaling Up of Non-Thermal Gliding Arc Plasma Systems for Industrial Applications." Plasma Chemistry and Plasma Processing. 42 1: 35-50.
88. Van Alphen, S., et al. (2021). "Sustainable gas conversion by gliding arc plasmas: a new modelling approach for reactor design improvement." Sustainable Energy & Fuels. 5 6: 1786-1800.
89. Choi, J., et al. (2025). "Characterization of gliding arc discharge using H_2/Ar gas mixture." International Journal of Hydrogen Energy. 106: 888-895.

90. Sharma, M., et al. (2025). “Enhancement of ozone production by increasing number density of plasma channels in volume DBD using ceramic foam for water treatment and industrial applications.” Journal of Electrostatics. 135.
91. Ullah, S., et al. (2023). “Recent Trends in Plasma-Assisted CO_2 Methanation: A Critical Review of Recent Studies.” Plasma Chemistry and Plasma Processing. 43 6: 1335-1383.
92. Li, J., et al. (2024). “Comparison of Ozone Production in Planar DBD of Different Modes.” Plasma Chemistry and Plasma Processing. 44 2: 891-905.
93. Liu, P., Song, Y., & Zhang, Z. (2021). “A Novel Dielectric Barrier Discharge (DBD) Reactor with Streamer and Glow Corona Discharge for Improved Ozone Generation at Atmospheric Pressure.” Micromachines (Basel). 12 11.
94. Sharma, S., & Maréchal, F. (2019). “Carbon Dioxide Capture From Internal Combustion Engine Exhaust Using Temperature Swing Adsorption.” Frontiers in Energy Research. 7.
95. Dimitrova, Z., & Maréchal, F. (2017). “Energy integration on multi-periods for vehicle thermal powertrains.” The Canadian Journal of Chemical Engineering. 95 2: 253-264.
96. Laurantzon, F. (2010). Flow Measuring Techniques in Steady and Pulsating Compressible Flows. Field, Department, Faculty, KTH.
97. Etheridge, D. W., & Sandberg, M. (1996). Building ventilation: theory and measurement. John Wiley & Sons Chichester, UK.
98. Enteria, N., et al. (2015). “Performance Test of Desiccant Heating, Ventilating and Air-Conditioning System by Using Multiple Tracer Gas Dilution Method.” International Journal of Air-Conditioning and Refrigeration. 23 04.
99. Havenith, G., et al. (2010). “Comparison of two tracer gas dilution methods for the determination of clothing ventilation and of vapour resistance.” Ergonomics. 53 4: 548-558.
100. Adachi, M., et al. (1997). “Measurement of exhaust flow rate: helium trace method with a mass spectrometer.” SAE transactions. 367-373.
101. Herget, W. F., et al. (1984). Progress in the prototype development of a new multicomponent exhaust gas sampling and analyzing system.).
102. Guragain, R. P., et al. (2021). “Influence of plasma-activated water (PAW) on the germination of radish, fenugreek, and pea seeds.” AIP Advances. 11 12.
103. Tang, X., et al. (2025). “A parameter measurement method for DBD-type ozone generators based on data fitting.” Measurement. 256.
104. Tański, M., et al. (2023). “Ozone Generation by Surface Dielectric Barrier Discharge.” Applied Sciences. 13 12.
105. Sung, T. L., et al. (2013). “Effect of pulse power characteristics and gas flow rate on ozone production in a cylindrical dielectric barrier discharge ozonizer.” Vacuum. 90: 65-69.
106. Restiwijaya, M., et al. (2019). “New development of double dielectric barrier discharge (DBD) plasma reactor for medical.” Journal of Physics: Conference Series. 1170 1: 012020.
107. Jõgi, I., Levoll, E., & Raud, J. (2016). “Plasma oxidation of NO in mixtures: The importance of back-reaction.” Chemical Engineering Journal. 301: 149-157.
108. Paulauskas, et al. (2019). “Application of Non-Thermal Plasma for NO_x Reduction in the Flue Gases.” Energies. 12 20.

109. Chen, Y., Wang, Q., & Wang, Y. (2024). “Analysis and Comparison of DBD Power Supplies With Different Control Methods.” IEEE Transactions on Plasma Science. 52 5: 1747-1757.
110. Shaban, M., et al. (2024). “Advancing DBD Plasma Chemistry: Insights into Reactive Nitrogen Species such as NO_2, N_2O_5, and N_2O Optimization and Species Reactivity through Experiments and MD Simulations.” Environ Sci Technol.
111. Sumaiyah, S., et al. (2025). “Analysis of Low Frequency on Dielectric Barrier Discharge Plasma Reactor for Ozone Production.” Trends in Sciences. 22 4.
112. Jodzis, S., & Zięba, M. (2018). “Energy efficiency of an ozone generation process in oxygen. Analysis of a pulsed DBD system.” Vacuum. 155: 29-37.

VITA

Name	Phurin Chonpan
Thesis Title	Nitrogen Oxides Abatement from Flue Gas via Non-Thermal Plasma
Major Field	Automotive and Energy Engineering Technology
Biography	I was born in Chonburi Province, Thailand, in 2001. I earned my Bachelor of Engineering (B.Eng.) in Mechanical and Automotive Engineering Technology in 2022 from the Faculty of Engineering and Technology, King Mongkut's University of Technology North Bangkok (KMUTNB), Rayong Campus. I am currently in a master's degree in Automotive and Energy Engineering Technology at the College of Industrial Technology, KMUTNB.